LARGE AREA GROWTH OF 2D SEMICONDUCTOR MATERIAL

DEPOSITION OF 2D MoS_2 USING THE MAGNETRON SPUTTERING SYSTEM, TOGETHER WITH FABRICATION AND AB-INITIO STUDY OF MoS_2-NI METAL CONTACTS

Wu Yaze

A0094483W

Supervised By:

Dr. Wang Shijie

Table of Contents

1 LIST OF FIGURES 4

2 ABSTRACT 5

3 ACKNOWLEDGEMENTS 6

4 INTRODUCTION 7

4.1 TWO DIMENSIONAL MoS_2 7
4.2 GROWTH OF 2D MoS_2 8
4.2.1 *Existing methods* 9
4.2.1.1 Vapour Phase Deposition 9
4.2.1.1.1 Chalcogenization of predefined metal or metal oxide films 9
4.2.1.1.2 Chemical Vapour Deposition 10
4.2.1.1.3 Requirements on deposition environment 10
4.2.1.2 Thermal Decomposition 10
4.2.2 *Magnetron Sputtering* 10
4.2.2.1 Ambient Gas Source 11
4.2.2.2 Sample Stage 11
4.2.2.3 Sputtering gun 11
4.2.2.3.1 Target 11
4.2.2.3.2 Power Supply 11
4.2.2.3.3 Magnet 11
4.2.2.3.4 Cooling System 12
4.2.3 *Special Set-up Used in This Project* 12
4.2.4 *Advantages of Magnetron Sputtering System over Other Deposition Methods* 12
4.3 METAL CONTACTS 13
4.3.1 *Existing Research* 14
4.4 MOTIVATION 14
4.5 WORK SCOPE 15

5 METHODOLOGY 15

5.1.1 *Equipment* 15
5.2 DEPOSITION OF 2D MoS_2 18
5.3 CHARACTERIZATION OF DEPOSITED 2D MoS_2 18
5.3.1 *XPS* 18
5.3.2 *Raman Spectroscopy* 18
5.3.3 *Photoluminescence* 19
5.4 MoS_2-NI CONTACT FABRICATION AND CHARACTERIZATION 19
5.5 AB-INITIO CALCULATIONS 20
5.5.1 *The Hamiltonian* 20
5.5.2 *Born-Oppenheimer Approximation* 21
5.5.3 *Density Functional Theory* 21
5.5.4 *Local Density Approximation* 22
5.5.5 *Generalized Gradient Approximation* 22
5.5.5.1 Perdew-Burke-Ernzerhof Exchange Correlation 23
5.5.6 *Bloch theorem and plane wave basis sets* 23
5.5.6.1 Cut-off energy 24
5.5.7 *Pseudopotentials* 25
5.5.8 *K-Point Sampling* 25
5.5.9 *Ab-initio Calculation Parameters* 25

6 RESULTS AND DISCUSSIONS 26

6.1 THEORETICAL EXPECTATIONS OF VARIOUS PARAMETERS' ROLE IN DEPOSITION 26
6.1.1 *Sputtering power* 26
6.1.2 *Voltage current balancing* 28

6.1.3 Duration ... *28*
6.1.4 Substrate temperature ... *29*
6.1.5 Ambient Gas Pressure ... *29*
6.1.6 Sulphur Pressure ... *29*
6.2 SUMMARY OF THEORETICAL ANALYSIS AND ACTIONS PROPOSED ... 29
6.3 MoS_2 DEPOSITION PARAMETER OPTIMIZATION ... 31
6.3.1 XPS Results and Sulphur pressure Optimization ... *31*
6.3.2 Raman Spectroscopy Results and Optimization of Deposition Duration ... *33*
6.3.3 Photoluminescence of MoS_2 Monolayers ... *35*
6.4 METAL CONTACT STRUCTURES ... 37
6.4.1 Ab-initio Calculations ... *37*
6.4.1.1 Atomic Structures ... 39
6.4.1.2 Band structures ... 39
6.4.1.2.1 Conduction Band Minimum / Barrier Height ... 40
6.4.2 Empirical Results ... *42*
6.4.2.1 Thickness of Ni Deposited ... 42
6.4.2.2 Presence of NiS at low Ni coverage ... 43
6.4.2.3 XPS Valence band analysis for MoS_2-Ni structures ... 43
6.4.3 Comparison of Empirical and Ab-initio Calculation Results ... *47*
6.4.4 Results in Comparison with Those from Existing Research ... *48*
7 CONCLUSION ... 48
8 FUTURE WORKS ... 49
9 REFERENCES ... 51

1 List of figures

Figure	Description	Page
Figure 1	Obtained from Kappera, Voiry [19.] (a), (b), Crystal structures of the 2H and 1T phases, respectively. In the upper diagram, trigonal prismatic (a) and octahedral (b) coordinations are shown. The lower panel shows the *c-axis* view of single-layer TMD with trigonal prismatic (a) and octahedral (b) coordinations. Atom colour code: purple, metal; yellow, chalcogen.	8
Figure 2	Adopted from Kasap [45]. Schottky barrier formation as metal comes into contact with a semiconductor of a different electron affinity as the work function of the metal.	13
Figure 3	(left) Schematic representation (top view) of the sputtering equipment with in-situ XPS. The sulphur evaporator heats solid sulphur of 99.95% purity until sublimation, thus providing the gaseous sulphur required by the sputtering process. (right) Schematic representation (side view) of the deposition chamber area, showing the approximate mounting angles of the sputtering gun and sulphur evaporator	16
Figure 4	Photograph of a substrate mounted on the sample stage.	17
Figure 5	XPS spectra of samples deposited with different sulphur pressures ranging from 1.9×10^{-5} mbar to 2.8×10^{-5} mbar stacked from bottom to top. Metallic 1T phase of MoS_2 is visible for samples deposited under lower sulphur pressures and the intensity of the 1T phase peak diminishes when sulphur pressure is increased. All the samples are deposited at 750°C, 10W and 434V, with Argon pressures adjusted during deposition to maintain voltage.	32
Figure 6	Raman Spectra of samples deposited near optimum condition with different deposition durations. Excitation laser used is of wavelength 514 nm.	33
Figure 7	Raman Spectroscopy with an excitation wavelength of 514nm. Δ is defined as the Raman Shift difference between the E^1_{2G} and A_{1G} Peaks, which are used by Lee, Yan [54] to measure the thickness of the MoS_2 films deposited. Horizontal lines with notations in inverted commas are thickness references suggested by Lee, Yan [54], thickness reference adjusted for this study is marked without inverted commas. All samples are deposited at 750°C and 434V, with sulphur pressure kept near optimum value. A trend of increasing film thickness with respect to deposition time is obtained.	34
Figure 8	PL spectra of samples with different Δ, obtained using an excitation laser with a wavelength of 514nm. Substantial PL is only observed for the samples with Δ of 22.72 and 23.24, with PL of the former much stronger than that of the latter.	35
Figure 13	Valence Band spectra of MoS_2 monolayer and MoS_2-Ni samples of different Ni thickness. The d_{z^2} band, d-p band and S band are marked up in the diagram. The spectra are aligned at Mo3d5/2 core peak.	44
Figure 14	Determination of Ev for as-deposited MoS_2.	45
Figure 15	Determination of fermi edge of the MoS_2-Ni structure whose Ni deposition duration is 15s.	45
Figure 16	Graph depicting variation of ϕ_B against deposition time of Ni.	46
Figure 17	Estimating Ni deposition rate as 15s / ML, barrier height data from ab-initio calculations for $2MoS_2$ series is matched with experimental results. The dampened fluctuation is expected due to the two extra layer of MoS_2 present [65], but in general, the trend proves our assumption in 6.4.1.2.1 correct.	47

2 Abstract

Monolayer two-dimensional MoS_2 with direct band gap is successfully deposited using magnetron sputtering, with optimum deposition condition obtained at sulphur pressure of 2.3×10^{-5} mbar, substrate temperature of 750° C, sputtering power of 10W and sputtering voltage of 434V under an argon atmosphere of 7.6×10^{-4} mbar. 1T-phased MoS_2 is observed to be deposited for lower sulphur pressures. Deposition speed is estimated at 3 minutes per monolayer.

Ab-initio calculation performed on model MoS_2-Ni structures reveal strong surface reconstruction and MoS_2-Ni interactions for lower Ni coverage. Strong orbital hybridization is also observed for 1ML-MoS_2-nML-Ni systems. Schottky barrier heights measured using 2ML-MoS_2-nML-Ni system reveal a barrier height of 0.72eV when 1ML of Ni is positioned on top of MoS_2. A minimum in barrier height of 0.55eV is observed for 2ML Ni coverage. Barrier height for bulk Ni coverage is found to be about 0.7eV

Measurements from XPS valence band spectra confirms the results from ab-initio calculations but showing a similar trend for 1ML-MoS_2-nML-Ni systems, with more fluctuation in barrier height. NiS is observed from the XPS spectra, corroborating the observation of significant interaction between Ni and MoS_2 made in the ab-initio calculations. Initial barrier height is found to be 0.57eV, the minimum barrier height is observed at about 0.44eV and the bulk Ni barrier height is measured at about 0.77eV.

3 Acknowledgements

I would like to thank Dr. Wang Shijie for his kind supervision, Dr. Chai Jianwei for his insightful guidance and directions in the lab, Dr. Yang Ming for his kind help with respect to the VASP calculations, and Prof Feng Yuan Ping for his generous help in granting the necessary resources to conduct the ab-initio calculations.

I would also like to thank my parents for their continued support over irregular video calls, which have been encouraging me to continue working on this project whenever the going gets tough.

Deposition and characterization of the samples are conducted in Institute of Materials Research and Engineering (IMRE), Agency for Science, Technology and Research (A*Star)

The Ab-initio calculations are performed using Vienna Ab-initio Simulation Package (VASP) version 5.3.5.

4 Introduction

4.1 Two Dimensional MoS_2

Transition Metal Dichalcogenides (TMDs) are materials formed with one transition metal ion and two chalcogenide ions. This group of materials includes various interesting compounds such as MoS_2, $MoSe_2$, WS_2 and WSe_2, among which MoS_2 has acquired significant attention in the scientific community due to its much desirable physical and optoelectronic properties.

MoS_2 monolayers have electronic and optical properties that are markedly different from those of their respective bulk counterparts[1, 2, 3, 4], making them promising semiconductor materials for various applications such as nanoelectronics[5, 6, 7], optoelectronics[8], catalysis[9], photo-detection[10], photovoltaics[11], and photocatalysis[12]. Moreover, MoS_2's immunity to short channel effect makes it a significant player in the field of electronics[13, 14, 15], in which it is widely accepted that 2D materials will play an important role [16, 17, 18].

Within a unit cell of MoS_2, each Mo ion is sandwiched by two S ions in the vertical directions, forming a hexagonal lattice in the XY plane. Between the two-dimensional layers, the sheets of material are held together by Van Der Waals forces, much like that in the structure of graphite.

However, there are two phases available for MoS_2, namely the 2H phase, with trigonal prismatic coordination, and the 1T phase, with octahedral coordination. The latter exhibits metallic characteristics while the former is more thermodynamically stable and yields a noticeably stronger PL[19]. The structures of these two phases are shown in Figure 1.

Although the 1T phase is metastable, with a relaxation energy of ~1.0eV for conversion to the thermodynamically stable 2H phase [19, 20, 21, 22], it is found to exist in our deposited films and hence is worth mentioning up front. The 1T phase can be identified by its lower binding energies for its Mo 3d orbitals[19] and S 2p orbitals[23], observable in the XPS spectrum.

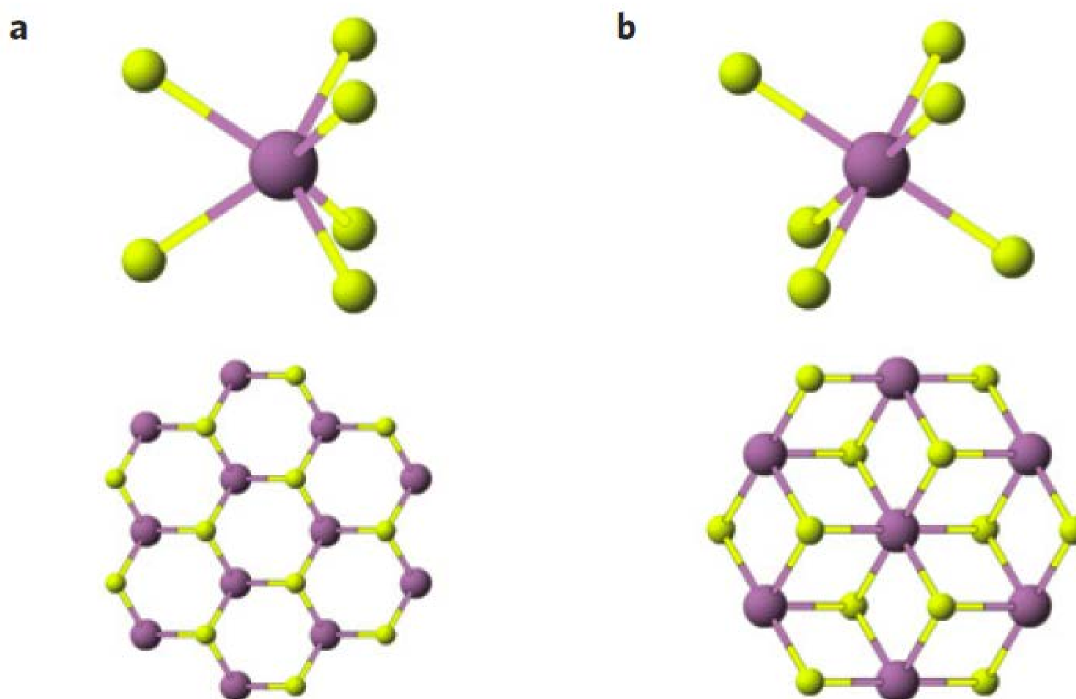

Figure 1 Obtained from Kappera, Voiry [19]. (a), (b), Crystal structures of the 2H and 1T phases, respectively. In the upper diagram, trigonal prismatic (a) and octahedral (b) coordinations are shown. The lower panel shows the *c*-axis view of single-layer TMD with trigonal prismatic (a) and octahedral (b) coordinations. Atom colour code: purple, metal; yellow, chalcogen.

In bulk form, MoS_2 possess an indirect band gap of 1.3eV that turns direct, with a band gap of 1.9eV, when it exists in monolayer[13, 15, 24, 25]. This tuning of electronic structure by thickness variation is attributed to quantum confinement.[25]

4.2 Growth of 2D MoS_2

The manufacturing of functional electronics requires the use of large area MoS_2 samples which need to be deposited through commercially viable deposition methods.

There are several approaches to obtaining monolayer MoS_2 thin films, most of which can be classified into two categories, namely top-down and bottom-up.

4.2.1 Existing methods

Top-down approaches are mostly inspired by those first used in the synthesis of graphene and involve mechanical exfoliation[26], laser[27], plasma[28], patterning methods[29] or thermal annealing[30]. These techniques are able to obtain high-quality MoS_2 flakes but with small grain sizes; they also require an already thin sample to work on, which is unfeasible for large-scale production.[31]

Bottom-up approaches include vapour phase depositions[32, 33, 34, 35, 36, 37], thermal decomposition [38], and magnetron sputtering [39]. These approaches are relatively scalable and will hence be discussed in detail.

4.2.1.1 Vapour Phase Deposition

Vapour Phase Deposition (VPD) relies on chemical reaction or physical transport of vaporized precursors to deposit MoS_2 onto a substrate; this category of processes can be further broken up into two methods: chalcogenization of predefined metal or metal oxide films[32, 33, 34, 35] and chemical vapour deposition[34, 36].

4.2.1.1.1 Chalcogenization of predefined metal or metal oxide films

Most of this type of MoS_2 fabrication methods uses solid precursors including MoO_3[32] or $MoCl_5$[33] to react with chalcogens carriers such S_8 or H_2S. However, such methods have been found to yield low carrier mobility of less than 0.1 $cm^2\ V^{-1}\ s^{-1}$ [34, 35], which is undesirable in device fabrication. Furthermore, the use of gas-phased precursor H_2S requires a cycle-based epitaxy, in which H_2S has to be vacated after one growth cycle before another cycle begins; this is to increase the island size of grown MoS_2[37]. This by no means is a complicated procedure for scaled-up set-ups.

4.2.1.1.2 Chemical Vapour Deposition

Chemical vapour deposition (CVD) is currently the more popular method to synthesize MoS_2 due to its simplicity, preference for monolayer growth and typically high sample mobility over 10 cm^2 V^{-1} s^{-1} [34, 36]

4.2.1.1.3 Requirements on deposition environment

The major drawback for VPD of MoS_2 is the limited spatial uniformity of the samples deposited[40], which can be mitigated by the use of pre-treated substrates[35, 36], seeding promoters[36, 41], atomic layer-deposited precursors[42], oxygen plasma treatment[43] and immediate-state precursors[44].

It can be observed from the amount of attention on precursors and seeding promoters that the growth mechanism of VPD for MoS_2 is heavily reliant on precursor properties as well as seeding mechanisms, which is a major shortcoming to the deposition method's scalability despite its relative success in depositing smaller scale samples.

4.2.1.2 Thermal Decomposition

MoS_2 can also be produced by thermal decomposition of $(\mathrm{NH_4})_2MoS_4$ [38], a process that involves one round of annealing in H_2 to obtain MoS_2 and another round of annealing at higher pressure and temperature to improve the sample's crystallinity and grain domain size.[38] A decent mobility of 4.7 cm^2 V^{-1} s^{-1} is reported.[38] However, the high temperature and vacuum required by this process renders it difficult to scale up, and a more robust system that relies less on high vacuum standards and temperature is needed.

4.2.2 Magnetron Sputtering

Magnetron sputtering is a form of Physical Vapour Deposition used for film deposition; it is made up of several key components, namely:

4.2.2.1 Ambient Gas Source

An ambient gas source usually supplies a noble gas to provide the noble gas ions required to bombard the target in order to release the target material to the substrate.

4.2.2.2 Sample Stage

The sample stage holds the substrate in place above the sputtering gun to collect the material deposited. The sample stage can be heated to provide the thermal energy to initiate or sustain the chemical reactions between participating species in the deposition process.

4.2.2.3 Sputtering gun

The sputtering gun comprises the following components:

4.2.2.3.1 Target

The target is usually a component of the material to be deposited.

4.2.2.3.2 Power Supply

The power supply supplies the necessary voltage to ionize the ambient noble gas atoms to cations and electron. The cations are electrostatically attracted to the negatively biased target and bombards the target with enough energy to eject some target material onto the substrate, through the ambient gas which may comprise some intentionally added reactive gas species to initiate reaction with the ejected target material to form the desired material on the substrate. A Direct current (DC) power supply is used for conducting targets and a Radio Frequency (RF) power supply is used for dielectric targets.

4.2.2.3.3 Magnet

The magnet provides the magnetic field that confines the charged particles near the sputtering gun so that these particles' mean free paths increase dramatically and they

hence have higher chances of bombarding into more ambient gas atoms to produce even more charged particles, therefore increasing the efficiency of the sputtering process.

4.2.2.3.4 Cooling System

Necessary cooling systems are attached to the sputtering gun to extract the heat produced during the sputtering process.

4.2.3 Special Set-up Used in This Project

In this project, a specially modified magnetron sputtering system is used to deposit single crystal MoS_2 samples of dimensions $2cm \times 1cm$, which is limited only by the geometry of the sample stage in use.

This very sputtering set-up has been specially modified to include a sulphur evaporation module, which heats elemental sulphur till sublimation, hence providing sulphur for the deposition of MoS_2. It also offers a low deposition rate, which is more favourable towards deposition of two-dimensional structures; details are discussed in 5.1.1.

4.2.4 Advantages of Magnetron Sputtering System over Other Deposition Methods

In comparison with other available deposition techniques, especially to CVD, magnetron sputtering technique does not require raising the temperature of a large amount of space, atmosphere or number and mass of components inside the set-up, making it considerably more scalable than other methods. Moreover, as target materials are sputtered directly onto the substrate, the supply of the material reaching the substrate is precisely controlled, offering great controllability to the deposition parameters as compared to CVD and other techniques. Furthermore, the magnetron sputtering process produces species of higher energy, which are readily able to react chemically with those in the chamber's atmosphere, hence does not involve the use of

precursors and the seeding mechanism, making it much simpler in terms of growth mechanism, and thus much easily scalable.

4.3 Metal Contacts

Despite the impressive characteristics of the MoS_2 as discussed in 4.1, it is essential to connect the fabricated MoS_2 device to an existing circuit for it to be useful. This brings about the issue of the metal contact between the MoS_2 device and the circuit.

A Schottky barrier is usually formed when a MoS_2 film is connected to a metal contact. This is due to the depletion region formed due to the different work functions of the metal and semiconductor[45], as seen in Figure 2. The presence of the Schottky barrier introduces electrical resistance, which leads to undesirable effects such as energy inefficiency.

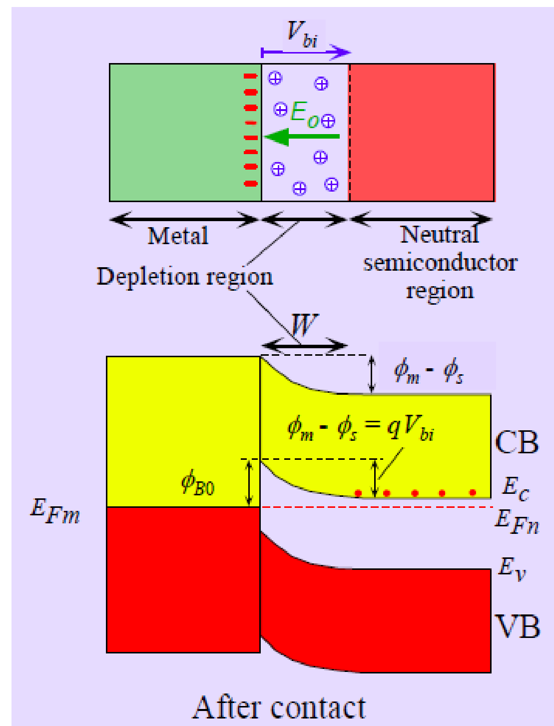

Figure 2 Adopted from Kasap [45]. Schottky barrier formation as metal comes into contact with a semiconductor of a different electron affinity as the work function of the metal.

Attempts to mitigate the Schottky barrier has revealed that the mechanism of the formation of Schottky barrier is not straight forward, as fermi-level pinning inhibits significant change in Schottky barrier height despite adjustments made to work functions of the metal. [46]

Therefore, it is of technical importance and academic interest that the topic is confronted.

4.3.1 Existing Research

Previous researches try to mitigate the Schottky Barrier problem by choosing metals of different work functions for the metal contacts, all of which achieved limited success[14, 47]. Scandium, which so far has been the best metal candidate, managed to achieve a barrier height of 30meV [14], which is still far from satisfactory.

Other methods involving gas[48] and charge transfer based molecular doping[49] on MoS_2 flakes lower the contact resistance at the expanse of degradation of on/off performance.

Insertion of interface layers such as MgO [50] and graphene[15, 51] interface layers is also proposed, but the air instability of the chemical doping approach makes it unsuitable for realizing reliable low resistance Ohmic contacts[52]. Complexity in manufacturing such a complex device is also a key issue against the scalability of the method.

4.4 Motivation

Despite the encouraging physical properties of MoS_2, it is still a challenge to successfully produce wafer sized samples that can be used for device fabrication and testing.[31] Many existing deposition techniques are limited in scalability by the requirements of precursors and seeding mechanism. As magnetron sputtering is able to circumvent the hurdles presented by precursors and seeding while still being able to deposit wafer scale samples, its capabilities motivate this study to achieve successful

deposition of large samples of MoS_2, which is of significant importance and forms the basis for further research on its physical and electronic properties.

The current struggle to obtain a good metal contact for the MoS_2-based devices, despite attempts of using different metals and interface materials, motivates this study to find a new way to control metal work functions by varying the thickness of the metal, which should prove useful for future works in improving the MoS_2 metal contacts.

4.5 Work Scope

In this study, Magnetron-sputtering deposition of 2D MoS_2 thin films of < 5 monolayers (ML) thickness is conducted. Deposition parameters are optimized and the deposited samples are characterized using XPS, Raman Spectroscopy, and PL.

Nickel is chosen as the contact metal and monolayer MoS_2 as the semiconductor.

Changes in Schottky barrier height caused by application of a different number of layers of nickel deposited on MoS_2 monolayer is studied through analysis of the valence band XPS spectra of the MoS_2-Ni contact structure.

Ab-initio calculations are also performed on Vienna Ab-initio Simulation Package (VASP) to study the physical configurations, the density of state, band structure of the contact structure, providing a theoretical study of the MoS_2-Ni metal contact structure.

5 Methodology

5.1.1 Equipment

The sputtering set up is a high vacuum magneto-sputtering equipment connected to a DC power supply and is equipped with an elemental sulphur evaporator, a heated

sample stage and a 4-inch circular sputtering gun holding a molybdenum target; Argon as the ambient gas is supplied to the set up through a hose with a flow control valve.

The sputtering set up is also connected with an XPS set-up, which can provide in-situ analysis of the deposited samples without them being exposed to atmospheric air. The samples are transferred from one set-up to the other through a transfer channel linking the two setups, as seen in Figure 3 below:

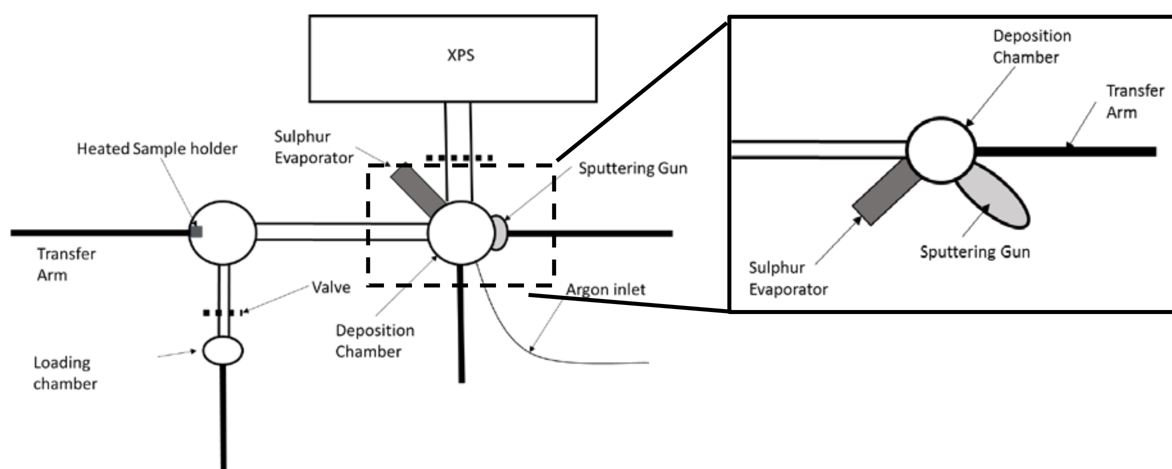

Figure 3 (left) Schematic representation (top view) of the sputtering equipment with in-situ XPS. The sulphur evaporator heats solid sulphur of 99.95% purity until sublimation, thus providing the gaseous sulphur required by the sputtering process. (right) Schematic representation (side view) of the deposition chamber area, showing the approximate mounting angles of the sputtering gun and sulphur evaporator

The substrate, 100nm of SiO_2 on <100> Si, is cut into $2.5cm \times 1.0cm$ pieces and is washed in acetone, followed by ethanol, and then DI water in ultrasonic wash for five minutes each to wash off any organic and inorganic contaminant. A clean substrate is then mounted onto the sample stage as shown below:

The Si-based substrate is a semiconductor that heats up when DC current is passed through the sample stage from one clamp to the other, hence achieving sample heating.

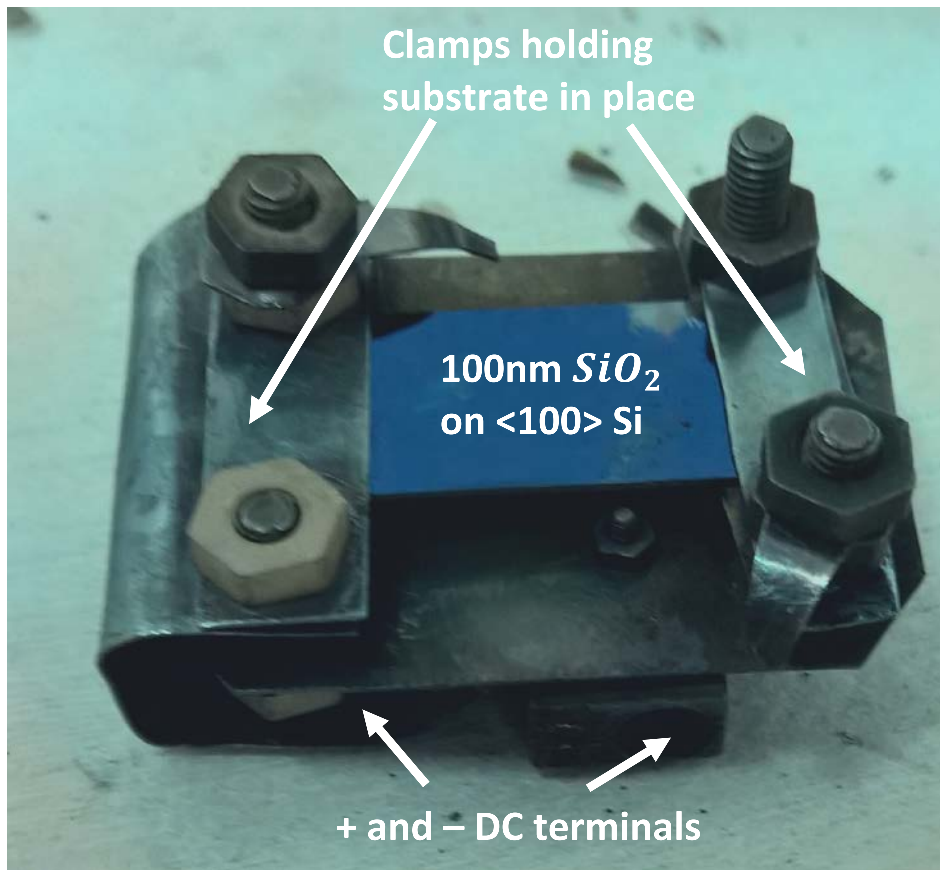

Figure 4 Photograph of a substrate mounted on the sample stage.

The sample holder is then placed into the sputtering set up and pre-heated up to a temperature of about 300° C and at pressure of about 1×10^{-6} mbar before argon and gaseous sulphur are introduced for the sputtering process to begin. Raising the substrate temperature is to prevent any unintended condensation of sulphur onto the substrate before sputtering.

Solid elemental sulphur of 99.95% purity is heated in the sulphur evaporator till sublimation to provide the sulphur gas required for the deposition of MoS_2. The pressure of the sulphur gas in the sputtering chamber is controlled by the electric power supplied to the evaporator. The valve on the sulphur evaporator is not used to control the supply of sulphur into the sputtering chamber as experience reveals that closing the

valve leads to impurity accumulation in the sulphur gas released, consequently adversely affecting the quality of the samples deposited.

5.2 Deposition of 2D MoS_2

MoS_2 samples are deposited at various substrate temperatures, sulphur pressures, argon pressures, deposition powers and deposition voltages to find the optimum condition to produce high-quality mono/multi-layers.

5.3 Characterization of deposited 2D MoS_2

Deposited samples are characterized for thickness, elemental composition, and photoluminescence using X-ray Photoelectron Spectroscopy (XPS), Raman Spectroscopy and photoluminescence.

5.3.1 XPS

XPS is performed on a VG ESCALAB 220i-XLsystem using a monochromatic Al Kα source. The pass energy of the analyser was set to 10 eV for high measurement resolution. Data from XPS is used to analyse the elemental composition and bonding condition of the deposited samples.

5.3.2 Raman Spectroscopy

Raman spectroscopy is performed on Horiba Scientific LabRAM HR Evolution Raman Spectrometer with a laser excitation wavelength of 514nm through a 100X optical microscope lens. It is used as the primary way of estimating the thickness of the deposited films. Thickness estimation using Raman spectroscopy for MoS_2 is done by correlating the Raman Shift difference between the E_{2g}^{1} mode (~385 cm^{-1}) and A_{1g} mode (~407 cm^{-1}) peaks to number of layers, with larger difference between the two peaks corresponding to more number of layers of MoS_2.[53]

Number of Layers	Approximate Raman shift difference / cm^{-1}
1	19.0 ± 0.5
2	21.5 ± 0.2
3	23.0 ± 0.1
4	24.1 ± 0.1
Bulk	25.2 ± 0.1

Table 1 Method of estimating number of layers of MoS_2 using Raman shift difference between E_{2g}^1 and A_{1g} peaks using a 514.5 nm excitation laser wavelength[54]as presented by Lee, Yan [54]

5.3.3 Photoluminescence

Photoluminescence studies are also carried out on the Horiba Scientific unit. PL is a strong indicator of the monolayer nature of the deposited MoS_2. This is due to the band structure of MoS_2 changing from indirect in multilayers to direct in monolayer [8, 11, 55]. Photoluminescence is also an indicator that the film deposited is of 2H phase and of good crystalline quality[19].

5.4 MoS_2-Ni contact fabrication and characterization

Nickel is deposited onto a MoS_2 monolayer sample fabricated in Section 5.2 of this paper using Electron Beam Physical Vapour Deposition (E-Beam PVD) with a Ni flux of 20nA at a base pressure of 1×10^{-9} Torr. Nickel is deposited for 15s, 20s, 30s, 90s, 120s, and 180s on the same sample, with additional deposition duration added to the already performed duration. XPS spectra are collected using the XPS set-up onto which the E-beam PVD is mounted, hence, the sample is not contaminated with atmospheric elements between depositions. This ensures any change observed to be due to the deposited Ni only.

The fermi edge and valence edge of the deposited samples are obtained from the aligned valance band XPS spectra and the Schottky barrier height is calculated using the equation

$$\phi_B = E_G - (E_F - E_V)$$

Equation 1

Where ϕ_B is the Schottky barrier height; E_G is the band gap of the monolayer MoS_2 (1.87 eV); E_F is the fermi energy, obtained from the fermi edge; E_V is the valence edge, obtained from the valence edge.

5.5 Ab-initio Calculations

Ab-initio calculations are performed on Vienna Ab-initio Simulation Package (VASP) to model the physical structure and the electronic properties of the MoS_2-Ni system.

Ab-initio calculations, or first principle calculations, are fundamental calculations that do not depend on adjustable parameters. The current ab-initio calculations used in studying material properties involves several key aspects worth introducing.

5.5.1 The Hamiltonian

In a system of N electrons and n nuclei, the Hamiltonian of the system is given by

$$\widehat{\boldsymbol{H}} = -\frac{1}{2}\sum_{i=1}^{N}\nabla_i^2 - \frac{1}{2}\sum_{l=1}^{n}\nabla_l^2 + \sum_{i<j}^{N}\frac{1}{|\boldsymbol{r}_i - \boldsymbol{r}_j|} + \sum_{i=1}^{N}\sum_{l=1}^{n}\frac{Z_l}{|\boldsymbol{r}_i - \boldsymbol{R}_l|} + \sum_{l<j}^{n}\frac{Z_l Z_J}{|\boldsymbol{R}_l - \boldsymbol{R}_J|}$$

Equation 2

Where Z denotes the nuclear charge, **r** and **R** denote the position of the electrons and nuclei respectively. The first term and second terms are the kinetic energy of the electrons and nuclei respectively; the third, fourth and fifth terms are the electrostatic potential energies among the electrons, among the nuclei and electrons, and among the nuclei respectively.

However, a Schrodinger equation containing such a many-body Hamiltonian is very difficult to solve; this leads to several approximations being put forward.

5.5.2 Born-Oppenheimer Approximation

The Born-Oppenheimer Approximation asserts that due to the large differences in mass between the electrons and the nuclei, during an interaction, the electrons are able to move rapidly to positions where they achieve their lowest energy while the much heavier nuclei do not move much during the same duration of time. Therefore, it can be assumed that the electrons move instantaneously with respect to the motion of the nuclei, and the whole process can be treated as an adiabatic one. Thus, the interactions in Equation 2 involving nuclei can be neglected.

Hence, Equation 2 can be simplified through Born-Oppenheimer Approximation to

$$\hat{H} = -\frac{1}{2}\sum_{i=1}^{N} \nabla_i^2 + \sum_{i<j}^{N} \frac{1}{|\boldsymbol{r}_i - \boldsymbol{r}_j|} + \hat{\boldsymbol{V}}$$

Equation 3

Where V is the potential energy of electrons in an external potential V(r).

5.5.3 Density Functional Theory

After the proposal of the Born-Oppenheimer Approximation, Hohenberg and Kohn's proof of two theorems[56] pertaining to the electronic density ρ(r) is fundamental to the establishment of the Density Functional Theory (DFT).

Theorem 1: If the number of electrons in the system is conserved, the external potential V(r) uniquely determines the ground state electronic density $\rho_0(r)$.

Theorem 2: There exists a universal energy functional E(ρ) of the electronic density ρ(r), which takes on its minimum value with the correct ground state electronic density $\rho_0(r)$.

Kohn and Sham's proposal of the Kohn-Sham Equation[57] (Equation 4) maps a many-electron system to a single-electron system in an effective potential formed by other nuclei and adiabatically stationary nuclei, where the exact electron density can be obtained once the exact exchange-correlation functional E_{xc} is given.

$$\left[-\frac{1}{2}\nabla^2 + \int \frac{\rho(\boldsymbol{r}')}{|\boldsymbol{r}-\boldsymbol{r}'|} d^3\boldsymbol{r}' + \frac{\partial E_{xc}[\rho(\boldsymbol{r})]}{\partial \rho(\boldsymbol{r})} + V(\boldsymbol{r})\right]\Psi_i(\boldsymbol{r}) = \epsilon_i \Psi_i(\boldsymbol{r})$$

Equation 4

The Kohn-Sham Equation has to be solved self-consistently so that the occupied electronic states generate a charge density that produces the electronic potential that is used to construct the equation.

5.5.4 Local Density Approximation

Although Kohn-Sham equation has simplified the problem of modelling the dynamics of the particles greatly, the exchange-correlation functional (E_{xc}) still cannot be found exactly. To solve this problem, Kohn and Sham proposed the Local Density Approximation (LDA) to approximate the E_{xc} near the particle of interest.

$$E_{xc}[\rho(\boldsymbol{r})] \approx E_{xc}^{LDA}$$

Equation 5

The LDA assumes a homogeneous electron gas where the positive charge is spread homogenously throughout the space. Although this is not exact, it is a decent model on which calculations of acceptable accuracy can be performed.

5.5.5 Generalized Gradient Approximation

To improve the accuracy of LDA by accommodating the fact that real systems are not homogeneous, newer Exchange-Correlation potentials such as Generalized Gradient

Approximations (GGAs) are devised. GGAs in general captures both the local and semi-local information: electron density and its gradient at a given point.[58]

5.5.5.1 Perdew-Burke-Ernzerhof Exchange Correlation

Perdew-Burke-Ernzerhof Exchange Correlation (PBE) is a type of GGAs, it includes features such as local electron density and its gradient and second-order gradient, making it a highly accurate and computationally efficient functional. It is worth mentioning as it is used in this study.

5.5.6 Bloch theorem and plane wave basis sets

The problem of solving the Kohn-Sham Equation can be further simplified by the use of Bloch's Theorem (Equation 6), which asserts the periodic nature of material lattices.

$$U_k(\boldsymbol{r}) = U_k(\boldsymbol{r} + \boldsymbol{T})$$

Equation 6

Here, $U_k(r)$ is the potential at r, T is the translation vector.

The use of Bloch's theorem effectively decreases the size of the system from ~10^{23} atoms and even more electrons to the size of one or a few unit cells, greatly decreasing the amount of atoms and electrons needed for calculation, and therefore drastically lowering the associated computational cost.

Plane waves in the form of

$$\Psi_k(\boldsymbol{r}) = U_k(\boldsymbol{r}) e^{i\boldsymbol{k}\cdot\boldsymbol{r}}$$

Where

$$U_k(\boldsymbol{r}) = \sum_{\boldsymbol{G}} C_k(\boldsymbol{G}) e^{i\boldsymbol{G}\cdot\boldsymbol{r}}$$

Equation 7

is also used to take advantage of the Bloch's Theorem.

Combining Equation 7 with Equation 6, we obtain a planewave function in the form of

$$\Psi_k(\boldsymbol{r}) = \sum_{\boldsymbol{G}} C_k(\boldsymbol{G}) e^{i(\boldsymbol{G}+\boldsymbol{k})\cdot\boldsymbol{r}}$$

Equation 8

And the electronic wave function can be written as a sum of plane waves

$$\Psi_i(\boldsymbol{r}) = \sum_{\boldsymbol{G}} C_{i,\boldsymbol{k}+\boldsymbol{G}}(G) e^{i(\boldsymbol{G}+\boldsymbol{k})\cdot\boldsymbol{r}}$$

Equation 9

5.5.6.1 Cut-off energy

Kinetic energy obtained from the planewave basis is of the form $\frac{\hbar^2}{2m}|\boldsymbol{k}+\boldsymbol{G}|^2$, and according to Bloch's Theorem, electronic wavefunctions at each k in the Brillioun zone can be expanded in terms of a discrete planewave basis set. As we are interested only in the ground state of the system, we only need plane waves of lower energies to obtain a reasonably accurate solution. This leads to the concept of a cut-off energy, which is the energy above which we dictate as not economical to calculate for a reasonably accurate solution.

5.5.7 Pseudopotentials

Although electronic wavefunctions can be expanded in terms of a discrete planewave basis set, the method is handicapped due to the large number of plane waves required to perform an all-electron calculation. Number of planewaves dictates the size of the Kohn-Sham Matrix to diagonalize.

Hence, pseudopotentials are used to decrease the number of electrons needed for the calculation by merging charge carried by the non-interacting core electrons into the charge of the nuclei and forming an equivalent charge, therefore dramatically decreasing the number of electrons involved in the calculations. And hence, leading to a much smaller number of planewaves needed for the calculations.

5.5.8 K-Point Sampling

Important information such as total energy and change density are determined by integration over the first Brillouin zone, which is a range of k-points. Numerical integration over the first Brillouin zone converges with increased number of k-points used, indicating an improved accuracy. However, the higher the number of k-points used, or the denser the k-mesh used, the higher the computational cost.

5.5.9 Ab-initio Calculation Parameters

Simulations of the Ni-MoS_2 metal contact structure is performed using VASP on a $2 \times 2 \times 1$ MoS_2 - $\sqrt{7} \times \sqrt{7} \times 1$ Ni superlattice, with a cut-off energy of 500eV and a K-point mesh density of $6 \times 6 \times 1$. A compressive strain of 2.2% is applied to the Ni and is found to not affect the band structure and work function of Ni significantly Work function of Nickel found in this model is about 5.06eV, close to the actual value of 5.35 for <111> Ni[59]. Simulation is spin polarized and Van der Waals interactions are taken into account.

Projector-augmented-wave (PAW) potential with 4p electrons of Mo and 3p electrons of Ni described as valence are used, while a regular PAW potential is used for S.

The exchange-correlation functional is treated using the Perdew-Burke-Ernzerhof (PBE) generalized-gradient approximation (GGA).

6 Results and discussions

6.1 Theoretical expectations of various parameters' role in deposition

The deposition of MoS_2 involves six different independent parameters, hence, the process of optimizing the deposition parameters is based on a series of educated deductions followed by empirical data rather than a large systematic pool of empirical data alone.

The independent variables involved in the deposition process include sputtering power, sputtering current, deposition time, substrate temperature, sulphur pressure and argon pressure. A discussion of each of their theoretical effects on the deposition process is necessary to facilitate the upcoming analyses.

6.1.1 Sputtering power

Sputtering power is an independent variable that determines the amount of energy being delivered to the sputtering gun per unit time. From the discussion in 4.2.2.3.2, we understand that this power is used to ionize the noble gas (for this case, Argon) in the sputtering chamber and to attract them into bombarding the molybdenum target, ejecting the material through the sulphur filled Argon atmosphere and onto the substrate. The power is hence translated into electrical potential energy of the Argon ions multiplied to the flow of these ions per unit time, as expressed in the equation below

$$\boldsymbol{P = IV = \frac{nq}{t} \cdot V = \frac{n_{AR^+}}{t} \cdot KE_{Ar^+}, where\ KE_{Ar^+} = eV}$$

Equation 10

The electrical potential energy of the argon cations is then converted into their kinetic energy (KE) as they are electrostatically attracted towards the target and bombard the target with an energy of eV, where e is the elemental charge possessed by the Ar^+ and V is the potential difference between the cations and the negative anode. In a very simple model, where we assume near-elastic collision between the Ar^+ and the metal target, kinetic energy of the released target material will be nearly equivalent to the kinetic energy of the incoming Ar^+ ions. Hence, target materials are released at power P, with a fraction of this material reaching the substrate.

Hence, Equation 10 can be extended as follows

$$P_{supplied} = P_{Ar^+} = P_{Mo} = \frac{n_{Mo}}{t} \cdot KE_{Mo}, where\ KE_{Mo} = eV$$

Equation 11

Increasing power supplied leads to both higher amount of metal ejected towards the substrate and higher energy of these metal species, both of which are not desirable for two-dimensional material growth, which prefers a slow and less energetic process.

Besides increased flux and energy of the ejected metal, increasing the power supplied also leads to a more inhomogeneous bombardment of the target. This is due to the higher current discrepancy across the radius of the target when a high power rating is used.[60] At higher power, the plasma glow on the target forms a bright ring, while at lower power, the plasma glow fills the entire target. The latter understandably leads to a more homogenous distribution of flux of the metal species ejected across the target, which is desirable for controlled growth of 2D MoS_2 films.

Therefore, power supplied should be minimized.

6.1.2 Voltage current balancing

Voltage is a dependent variable of power supplied, argon pressure and sulphur pressure. However, as voltage can be monitored in real time during the deposition process, it is a good indicator of the conditions inside the deposition chamber; its variations can prompt timely adjustment of the corresponding independent variables to maintain the optimum deposition conditions.

As discussed in 6.1.1, the voltage supplied should be kept small to minimize the kinetic energy of the ejected metal species, and this can be done mainly by minimizing the power supplied. In addition, as the power supply controls only power, voltage, and current distribution have to be managed through some other means, namely through varying argon pressure and sulphur pressure, whose effects will be discussed later.

At a given power, lowering the voltage increases the current and current discrepancy across the radius of the target, which, as discussed in 6.1.1, is not desired. Hence, the voltage at a minimized supplied power should be tuned carefully to ensure a low current and current discrepancy across the radius of the target as well as a low energy of the molybdenum ejected from the target. A relatively homogeneous plasma discharge on the target should be the bottom-line for the balancing of voltage and current for a given supplied power.

6.1.3 Duration

Duration is an independent variable that most effectively controls the amount of material deposited. Hence, deposition duration is correlated with the number of layers deposited in this study.

6.1.4 Substrate temperature

Theoretically, higher substrate temperature increases the kinetic energy of the ions deposited onto the substrate, allowing them to relax more completely and thus leading to a better quality of the material deposited. Hence, the temperature of the substrate should be maximized. As the maximum reachable temperature of the sample stage is 750 °C, the substrate temperature is fixed at 750°C.

6.1.5 Ambient Gas Pressure

Argon, as the ambient gas in the deposition chamber, is the source of Ar^+ ions that is responsible for the ejection of metal species to be deposited onto the substrate. The concentration or pressure of argon is, therefore, positively related to the current, hence making it an independent variable to the control of voltage at a given power supplied.

6.1.6 Sulphur Pressure

Sulphur is a reactive species; therefore, it will lead to a drastic decrease of the erosion rate of the target and as such in a drastic decrease of the deposition rate.[61] This translates into a higher voltage for a given power supplied.

As Sulphur is an element making up MoS_2, its pressure has to be optimized according to the requirement of the film quality. However, as sulphur is sublimed from the evaporator, its pressure is not as easy to control as that of argon; therefore, real-time maintenance of constant voltage is done by varying the argon pressure while keeping the sulphur pressure constant.

6.2 Summary of theoretical analysis and Actions proposed

The theoretical hypotheses proposed in 6.1 simplifies the 6-dimensional parameter optimization exercise into a 3 dimensional one, with the variables left to optimize being

duration, argon pressure, and sulphur pressure; the latter two variables determine the voltage, which is used as an indicator for real-time adjustment of deposition condition. Hence, the 3 dimensional optimization process can be further divided into two sub-processes: a two dimensional quality optimization process and a one dimensional thickness optimization process, both of which are much more manageable than the original 6-dimensional problem.

Variable	Action
Power Supplied	Minimize
Voltage	Tune to sustainable homogeneous discharge voltage
Duration	Correlate with number of layers deposited
Substrate Temperature	Maximized at 750°C
Argon pressure	Optimize and adjust in real time during deposition to fix voltage
Sulphur pressure	Optimize w.r.t. film quality

Table 2 Tabulation of experimental variables available. Underlined variables are to be optimized.

6.3 MoS_2 Deposition Parameter optimization

6.3.1 XPS Results and Sulphur pressure Optimization

As the sputtering mechanism requires a minimum power and voltage to initiate and then maintain the sputtering process, the power supplied is kept at 10W, below which premature termination of the sputtering process begins to occur. With power minimized, voltage is set at 434V, at a point where plasma glow on the target is visually homogeneous. Initial deposition time is fixed at 120s.

With voltage fixed, sulphur pressure becomes the only independent variable to optimize with respect to the quality of the sample produced. The quality of the sample can most generally be verified through analysis of the bonding conditions of molybdenum ions by XPS.

As 2H phased MoS_2 is desired over the metallic 1T phased MoS_2, the presence of the latter is closely monitored using XPS.

It is observed that peaks of 1T phase MoS_2 are present in XPS spectra of samples deposited with lower pressures of sulphur, with the intensity of the peaks diminishing with increasing sulphur pressure, as seen in Figure 5. The peaks of 1T phased MoS_2 eventually disappears at sulphur pressure of 2.3×10^{-5} mbar, leaving behind

symmetric Mo3d peaks. The corresponding Argon pressure to this sulphur pressure is 7.6×10^{-4} mbar.

We hence believe that 2.3×10^{-5} mbar is the threshold sulphur pressure above which concentration of 2H phased MoS_2 become dominant. Therefore, the deposition perimeter should be optimized to this sulphur and argon pressure.

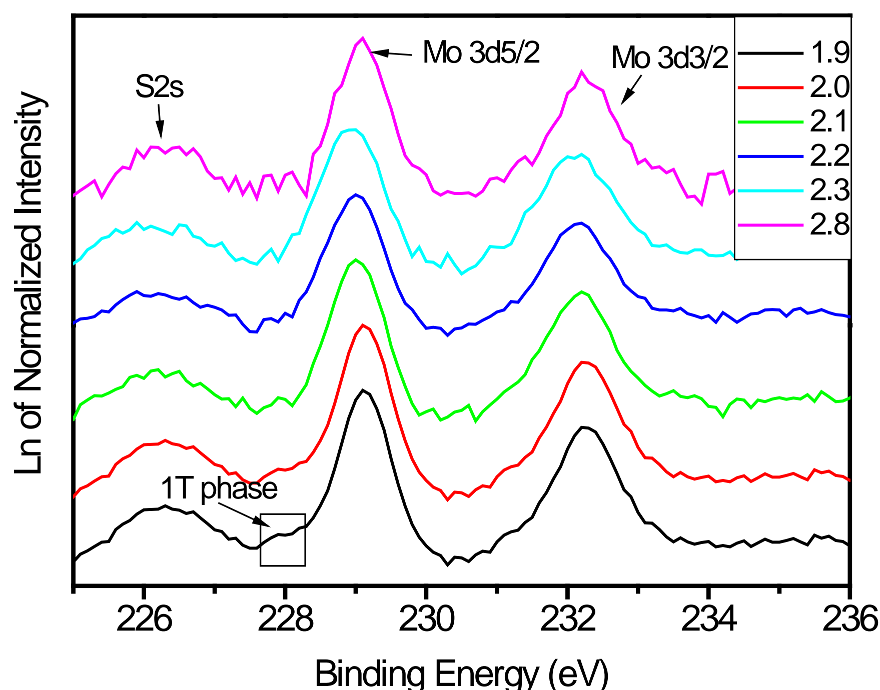

Figure 5 XPS spectra of samples deposited with different sulphur pressures ranging from 1.9×10^{-5} *mbar* to 2.8×10^{-5} *mbar* stacked from bottom to top. Metallic 1T phase of MoS_2 is visible for samples deposited under lower sulphur pressures and the intensity of the 1T phase peak diminishes when sulphur pressure is increased. All the samples are deposited at 750°C, 10W and 434V, with Argon pressures adjusted during deposition to maintain voltage.

Therefore, in terms of quality of the sample deposited, the optimum deposition parameters can be summarized as follows:

Sulphur Pressure	2.3×10^{-5}mbar
Substrate Temperature	750° C
Sputtering Power	10W
Sputtering Voltage	434V

Table 3 Optimum deposition parameters for MoS_2

However, it is important to note that due to the sublimation process, constant fluctuations in sulphur pressure is present and hard to predict and control, making it challenging to maintain and reproduce the optimum deposition condition. Despite our best efforts to approach the optimum deposition parameters, deposition at near optimum deposition conditions is more realistic.

6.3.2 Raman Spectroscopy Results and Optimization of Deposition Duration

With optimum deposition condition for MoS2 films finalized, the thickness of the films deposited can be correlated with the duration of deposition. A study of the Raman Spectra, as implemented by Lee, Yan [54], is performed on samples deposited near optimum conditions for different durations to obtain their thickness.

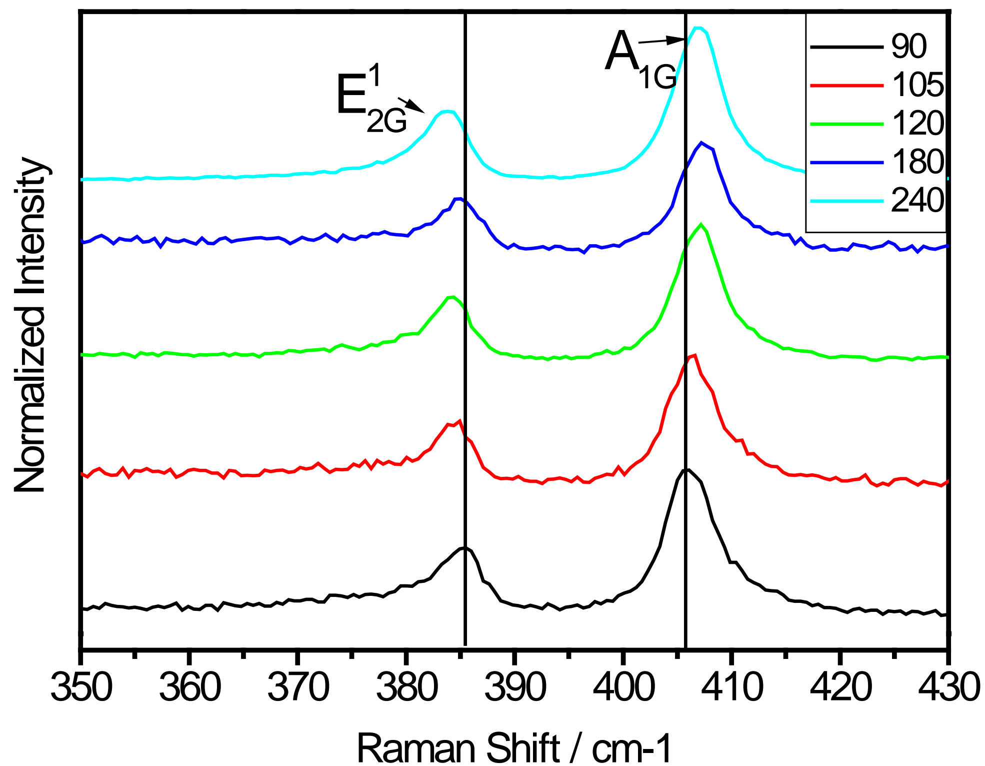

Figure 6 Raman Spectra of samples deposited near optimum condition with different deposition durations. Excitation laser used is of wavelength 514 nm.

It is observed that with increased deposition time, the E_{2G}^{1} peak shifts towards lower wave numbers while the A_{1G} shifts towards higher wave numbers, suggesting an increased film thickness with increased deposition time, which agrees with the results by Lee, Yan [54].

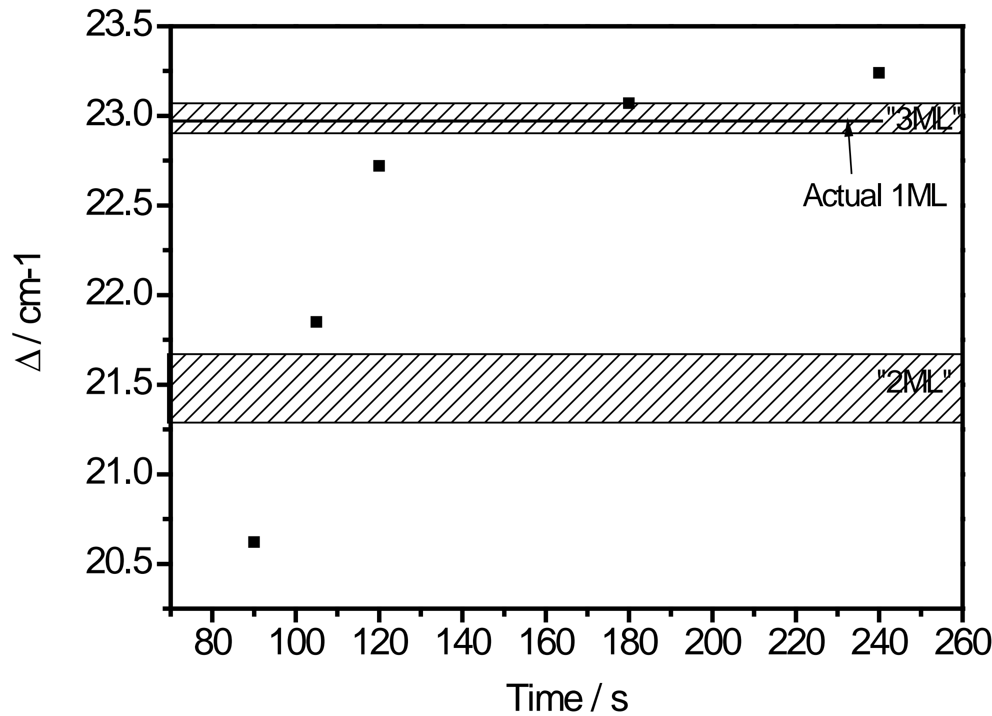

Figure 7 Raman Spectroscopy with an excitation wavelength of 514nm. Δ is defined as the Raman Shift difference between the E_{2G}^{1} and A_{1G} Peaks, which are used by Lee, Yan [54] to measure the thickness of the MoS_2 films deposited. Horizontal lines with notations in inverted commas are thickness references suggested by Lee, Yan [54], thickness reference adjusted for this study is marked without inverted commas. All samples are deposited at 750°C and 434V, with sulphur pressure kept near optimum value. A trend of increasing film thickness with respect to deposition time is obtained.

According to results from Lee, Yan [54], the thickness of the deposited films is in the range of sub-2ML to 3ML, as shown in Figure 7. This is a significant validation of the capability of the sputtering set up to produce low-dimensional MoS_2 films. With deposition duration between suggested sub-2ML and 3ML samples more than 120s apart, the sputtering set up offers excellent controllability of the thickness of the films deposited.

6.3.3 Photoluminescence of MoS_2 Monolayers

Considering the data obtained from PL, there is some doubt as to whether the results by Lee, Yan [54] is applicable to samples deposited using this sputtering set up. As seen from Figure 8, Photoluminescence (PL), which is a major indicator to monolayer MoS_2 films, only begins to emerge in samples with Δ >22.5 cm^{-1}, which corresponds to the thickness of >2.5ML in the work by Lee, Yan [54].

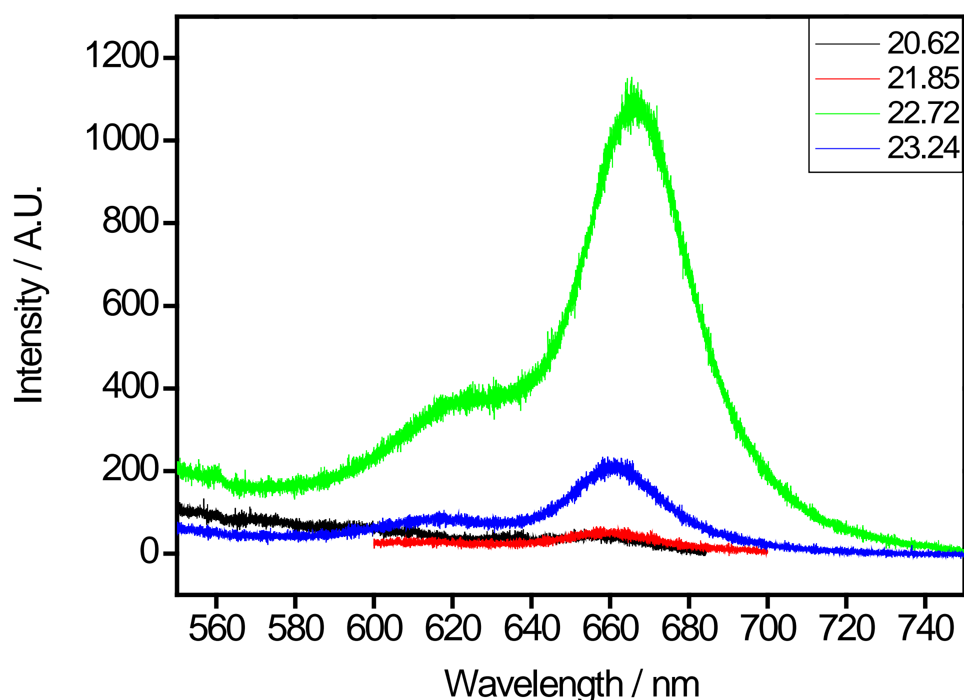

Figure 8 PL spectra of samples with different Δ, obtained using an excitation laser with a wavelength of 514nm. Substantial PL is only observed for the samples with Δ of 22.72 and 23.24, with PL of the former much stronger than that of the latter.

This discrepancy can be attributed to the higher concentration of defects present in the samples. As increased concentration of defects is known to cause a downshift of the position of the E' peak and an upshift of the position of the $A_1{}'$ peak[62], which leads to an increase in value of Δ for a given film thickness. As such, we should recalibrate the Δ value for a MoS_2 monolayer. The calibration is marked in figure 7.

Despite the increased concentration of defects in the samples produced by this method, a concurrent study has shown that devices built using samples synthesized on this set up are able to reach mobility of ~12.2 $cm^2 V^{-1}$ [31], comparable to devices built from mechanically exfoliated monolayers[32, 38, 41, 63, 64].

Significant photoluminescence is observed for Δ values of 22.72 cm^{-1} and 23.24 cm^{-1}, with the intensity of the former much stronger than that of the latter. This indicates that Δ =22.72 cm^{-1} is much closer to the monolayer regime than Δ =23.24 cm^{-1}. However, it should be noted that sample with Δ =21.85 cm^{-1} only shows marginal PL, suggesting that the maximum PL intensity should be expected from samples with Δ between 22.72 cm^{-1} and 23.24 cm^{-1}.

The sample with Δ=20.62 cm^{-1} has shown no significant evidence of PL; considering this together with the trend shown in Figure 8, we deduce that the sample is in the sub-monolayer regime.

Hence, we suggest an adjusted thickness/Δ relationship for the samples obtained using our magnetron set up, with the Δ of a monolayer MoS_2 deposited being around 23 cm^{-1}, the approximate average between 22.72 cm^{-1} and 23.24 cm^{-1}.

This adjustment to the result by Lee, Yan [54] further compliment the capability of the set up to deposit monolayer MoS_2 as a large duration of near 200s is needed for a monolayer, making control of the deposition process very manageable.

The main PL peaks of the samples correspond to a direct band gap of about 1.87eV, which is in good agreement with the band gap of a monolayer MoS_2 film found in the literature. [13, 15, 31]

6.4 Metal Contact Structures

6.4.1 Ab-initio Calculations

The 1-ML-Ni example of the superlattice used for the simulation is as shown in Figure 9 below. Systems with up to 5-ML-Ni and 2-ML-MoS_2 are used in this study, with structures sharing similar characteristics with the 1-ML-Ni example. It can be observed that the energy minimizing atomic positions for Ni are the top-sites.

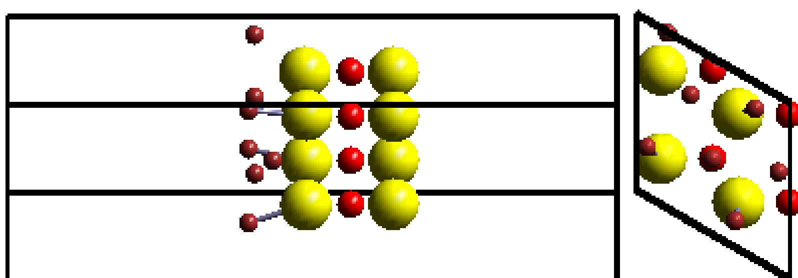

Figure 9 Relaxed lattice of the MoS_2-Ni contact structure used for VASP simulations. Nickel, sulphur, and molybdenum atoms are represented by small red spheres, large yellow spheres, and medium sized orange spheres respectively. (Left) superlattice as seen towards negative x direction. (Right) superlattice as seen towards negative z direction. Sufficient vacuum is provided in the z direction to prevent unintended inter-cell interactions.

The atomic structures, band structures, and density of states of the various samples are shown in Figure 10 below.

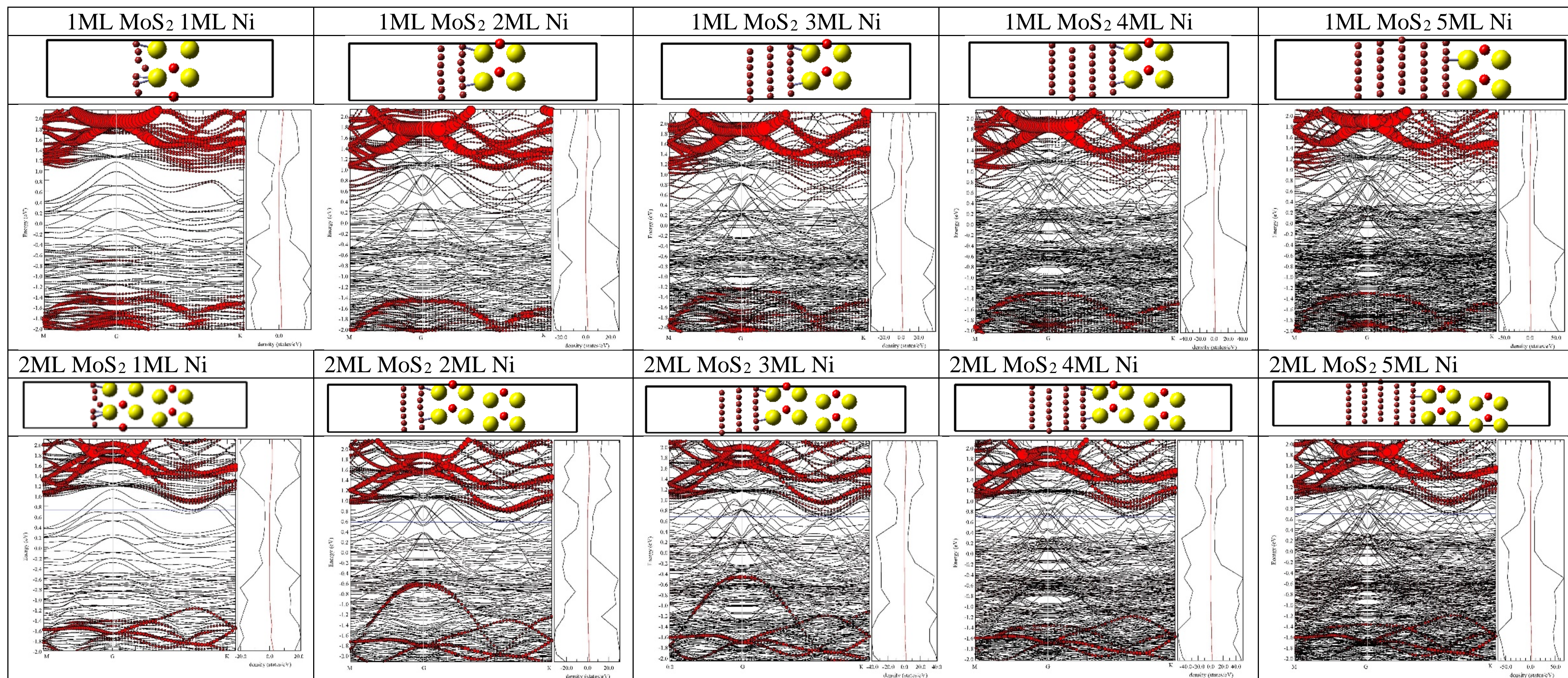

Figure 10 Tabulation of various MoS_2-Ni contact structures. First 3 rows belong to the 1ML-MoS_2 series while the last 3 rows belong to the 2ML MoS_2 series. The second row of each series shows the atomic structures of the systems, with small red spheres as nickel atoms, medium sized orange spheres as molybdenum atoms and large yellow spheres as sulphur atoms. The third row of each series shows the band structures of the systems. Bands marked with red circles are projected bands from MoS_2, taken from the plane of sulphur atoms furthest away from the nickel atoms; diameter of the circles are proportional to the weight of the K point. Density of States are tabulated vertically for each sample's band structure and are aligned with the energy axis. Fermi level is set to be 0eV. Conduction minima for 2ML MoS_2 series are marked using blue solid lines.

6.4.1.1 Atomic Structures

It is observed in Figure 10 that lower nickel coverage leads to more significant interactions among the nickel atoms and the MoS_2 layer, as seen from the larger number of bonds formed between the two different materials and the amount of reconstruction on the nickel surface when lower number of layers of nickel is present.

This is not unexpected as the thin coverage of nickel compels the nickel atoms to lower their energies by bonding with the sulphur atoms from the MoS_2 layer. This results in larger number of bonds formed between the nickel atoms and the MoS_2, as well as in surface reconstruction that involves nickel atoms moving closer to the MoS_2 layer for samples with less nickel coverage.

6.4.1.2 Band structures

Nickel deposited on MoS_2 monolayers have shown significant interaction with the MoS_2, leading to substantial orbital hybridization that spans nearly the entire energy spectrum from fermi level upwards. This leads to a great challenge in determining the calculated conduction band minimum (CBM) of the system.

Therefore, band structure for a nickel - bilayer MoS_2 system is calculated in an attempt to find out the relationship between Ni coverage and band structure of the system. We assume, based on empirical data discussed in 6.4.3, here that the results, in terms of trends in which the CBM varies, are the same for monolayer MoS_2 and bilayer MoS_2 systems. ϕ_B of bilayer MoS_2 systems are known to be smaller than monolayer MoS_2 systems,[65] thus we shall expect an underestimation of actual CBM values for 1ML-MoS_2 systems.

As observed in 1ML-MoS_2 series of Figure 10, although significant orbital hybridization makes quantifying ϕ_B difficult, it is not hard to see that the CBM of the

projected MoS_2 bands is closer to the fermi level than the valence band maximum (VBM) does. This puts monolayer MoS_2 systems as n-type, which is widely agreed upon both in experimental as well as ab initio results.[15, 65]

However, it is interesting to note that in the 2ML-MoS_2 series, Ni coverage of 2ML and 3ML is associated with the emergence of a new valence band centred about Γ, which puts the VBM equally spaced and closer to the fermi level than the CBM respectively, thus making the system intrinsic and p-type respectively.

Nevertheless, as the reason for the n-type-p-type conversion requires further studies that are beyond the scope of this paper, the 2ML-MoS_2 system is only used as a tool to estimate the CBM of the 1ML-MoS_2. Thus, for the sake of this study, we dictate ϕ_B as the difference between the CBM and the fermi level (0eV), which equals the value for CBM.

6.4.1.2.1 Conduction Band Minimum / Barrier Height

CBM for 2ML MoS_2 series systems is obtained by identifying the minima of the marked bands with appreciable weight.

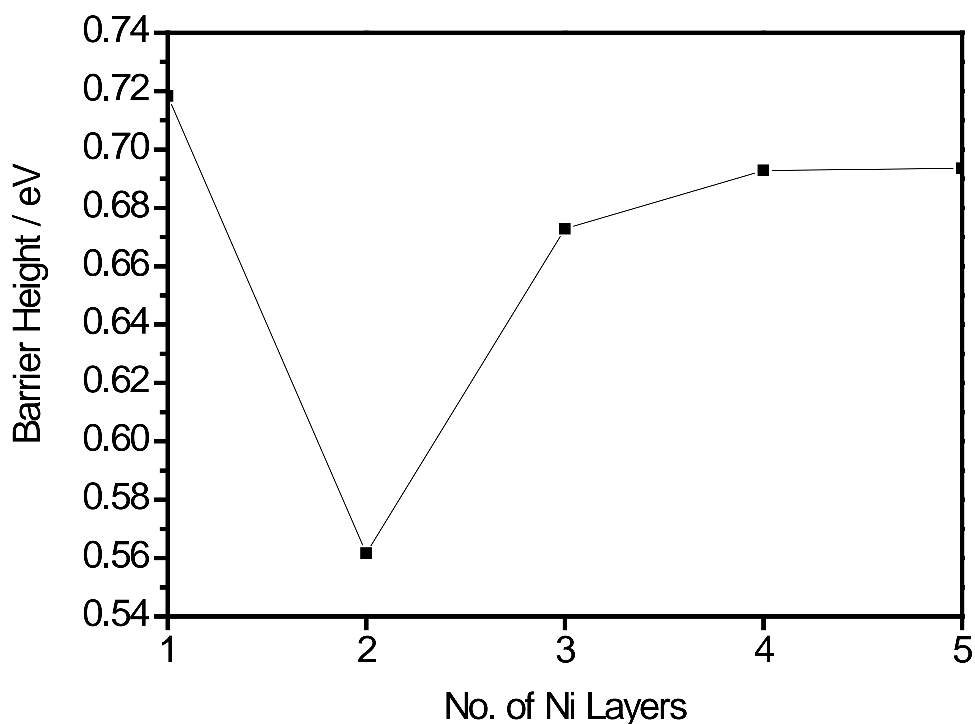

Figure 11 ϕ_B obtained from ab initio calculations using 2ML MoS_2 series. ϕ_B is observed to decrease before increasing to the bulk Ni-MoS_2 contact value of 0.7eV, which agrees well with data obtained from Leong, Luo [15].

It is noted that the barrier height decreases initially before rising again to reach the bulk Ni coverage value of about 0.7eV, which is also obtained by other studies. [15, 65]

The rising trend for the barrier height from 2ML of Ni onwards can be explained by the decrease in the amount of interaction between the MoS_2 layer and the nickel atoms when more nickel atoms are added. With more nickel atoms available, interfacial nickel atoms can bond with other nickel atoms, thus diluting their bonding with the MoS_2. This preferential interaction with other nickel atoms is visible in the lattice structure plots shown in Figure 10, where both number of bonds with MoS_2 and amount of surface reconstruction for nickel layers lessen when more nickel atoms are deposited.

The high barrier height observed for monolayer Ni coverage is suspected to be due to interfacial bonds formed among the Ni and S ions, leading to the formation of NiS. The details will be discussed in section 6.4.2.2.

6.4.2 Empirical Results

6.4.2.1 Thickness of Ni Deposited

In this study, we verify the thickness of the Ni deposited by observing the intensity of the Ni(acac)$_2$ satellite peak, which is 6eV away from the main Ni 2p3/2 peak in the XPS spectrum. Formation of the Ni(acac)$_2$ satellite peak is due to the interlayer bonds formed in the face-centred cubic lattice of Ni. Therefore, the presence of the satellite peak can be used as an indicator of the multi-layered nature of the Ni deposited.

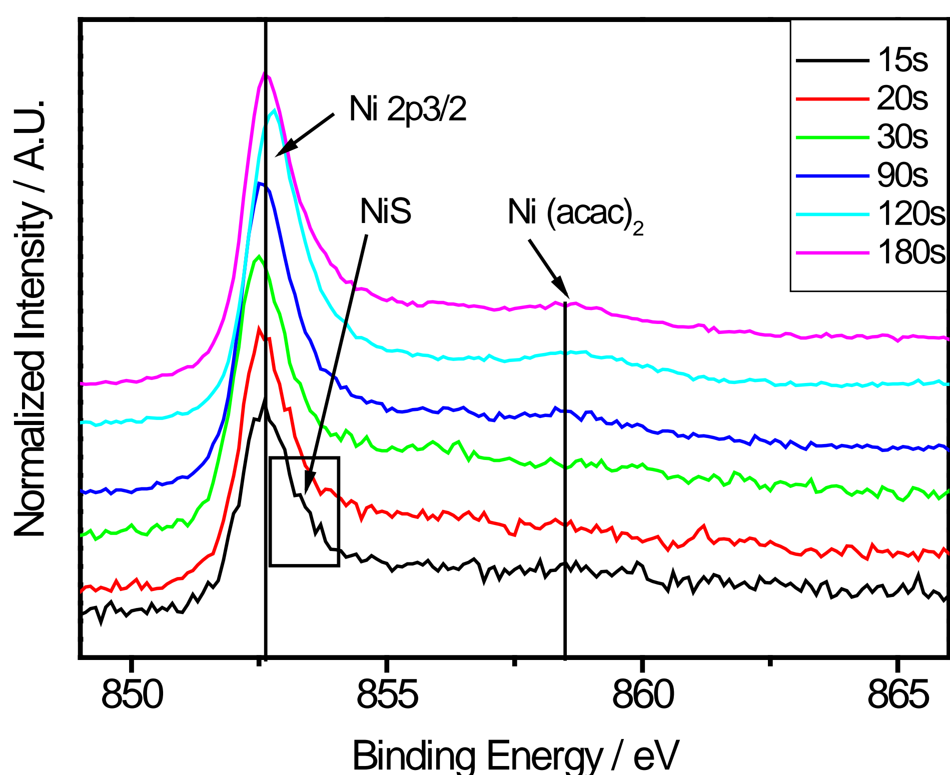

Figure 12 XPS spectra of Ni 2p3/2 peak and Ni(acac)$_2$ satellite peak. Satellite peaks are observed in samples with Ni deposition duration >15s, indicating >1ML coverage for these samples. Consequently, samples with 15*s* deposition duration can be considered to have monolayer and sub-monolayer Ni coverage. Peak corresponding to NiS structures is observed to be formed for near monolayer coverage.

It can be observed that the satellite peak is absent for Ni deposition duration of 15s while satellite peaks become increasingly prominent for longer Ni deposition durations.

Using the absence of satellite peak as an indicator of monolayer Ni coverage, we can say that for Ni deposition durations of less or equal to 15s, the Ni deposited is less or equal to a monolayer, while larger Ni deposition durations lead to multilayer coverage.

6.4.2.2 Presence of NiS at low Ni coverage

It is also observed from Figure 12 that NiS is formed at monolayer Ni coverage. The formation of NiS makes the Ni-MoS_2 system no longer as distinctly Ni and MoS_2, but a mix of Ni-MoS_2, NiS-MoS_2, and any other feasible combination.

As reports on electronic properties of NiS are scarce, it is hard to determine the exact mechanism behind the increase in barrier height observed for the sample with Ni monolayer coverage. However, it is highly suspected that the presence of NiS and the rise in barrier height for monolayer Ni coverage are correlated.

6.4.2.3 XPS Valence band analysis for MoS_2-Ni structures

The valence band spectrum of MoS_2 comprises three distinct regions, namely the d_{z^2} band at ~2.2 eV, the d-p band at 3 to 9 eV, and the S band at ~13.5 eV[66], which originate mainly from the nonbonding 4d electrons of Mo, the bonding states of hybridized Mo 4d and S 3p electrons, and the nonbonding S 3s electrons, respectively.[66]

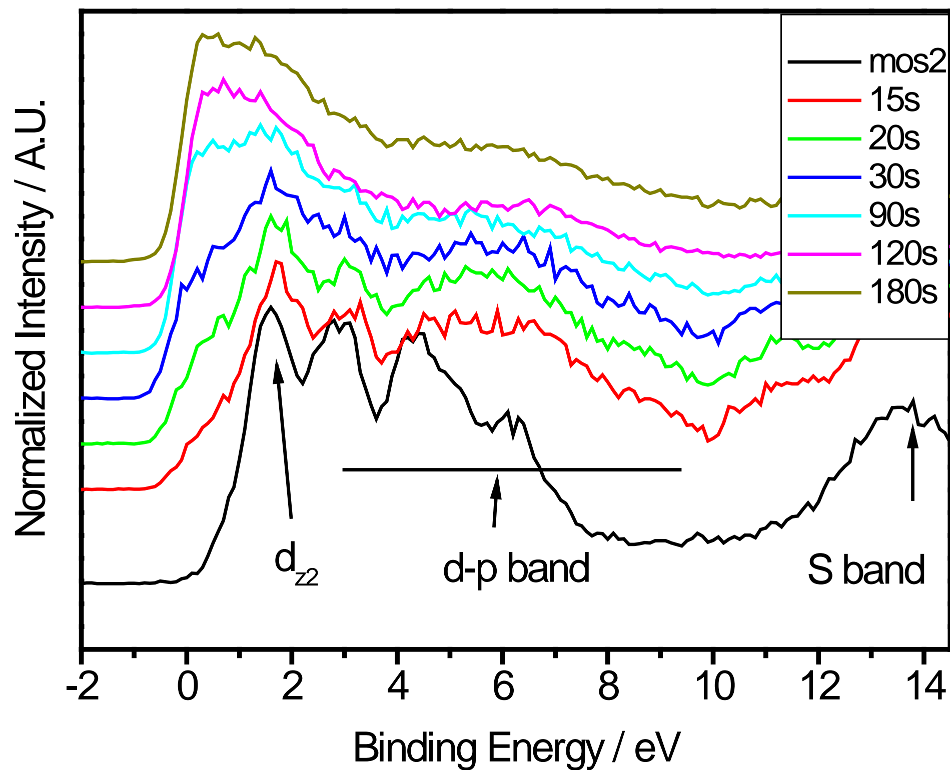

Figure 13 Valence Band spectra of MoS_2 monolayer and MoS_2-Ni samples of different Ni thickness. The d_{z^2} band, d-p band and S band are marked up in the diagram. The spectra are aligned at Mo3d5/2 core peak.

The valence edge of the MoS_2 monolayer is obtained by extrapolating the edge of the valence band spectra near 0 binding energy to the x-axis. Fermi edge of the MoS_2-Ni structure is obtained by extrapolating the valence peak near 0 binding energy to the x-axis, as shown in Figure 14 below.

Two manual measurements are taken for each valence edge and Fermi edge data point. The average of the measurements is calculated and error involved tabulated.

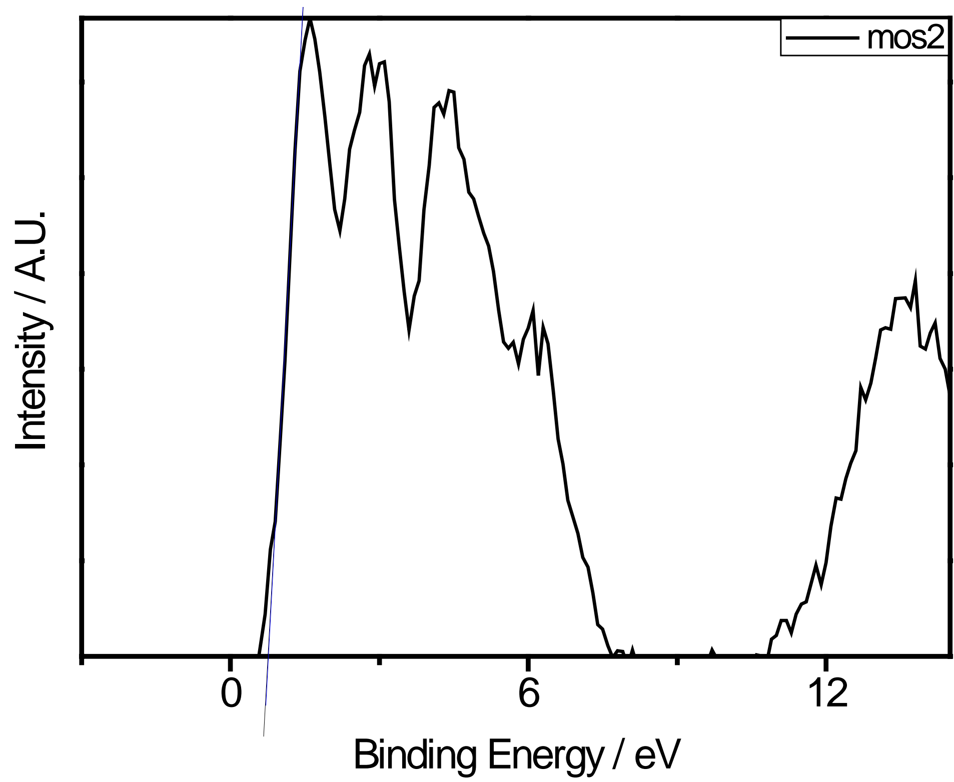

Figure 14 Determination of Ev for as-deposited MoS_2.

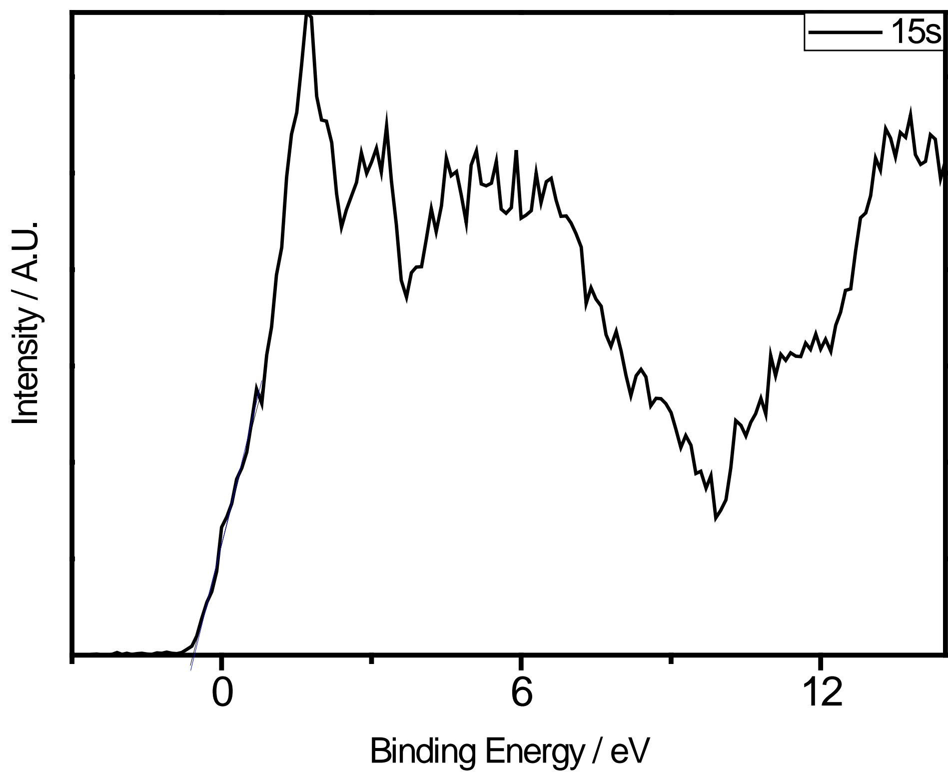

Figure 15 Determination of fermi edge of the MoS_2-Ni structure whose Ni deposition duration is 15s.

The valence edge of the MoS_2 monolayer is found to be $(-0.769 \pm 0.004)\ eV$, while the fermi edges of the metal contact structures range from about 0.32 eV to about 0.65eV. Assuming the difference in energy between valence edge and core level peak for Molybdenum is constant with or without the Ni overlayer[67], ϕ_B is observed, as shown in Figure 16, to initially decrease with increasing Ni thickness, but appears to reach a minimum of around 0.44 eV at 30s of Ni deposition before increasing again.

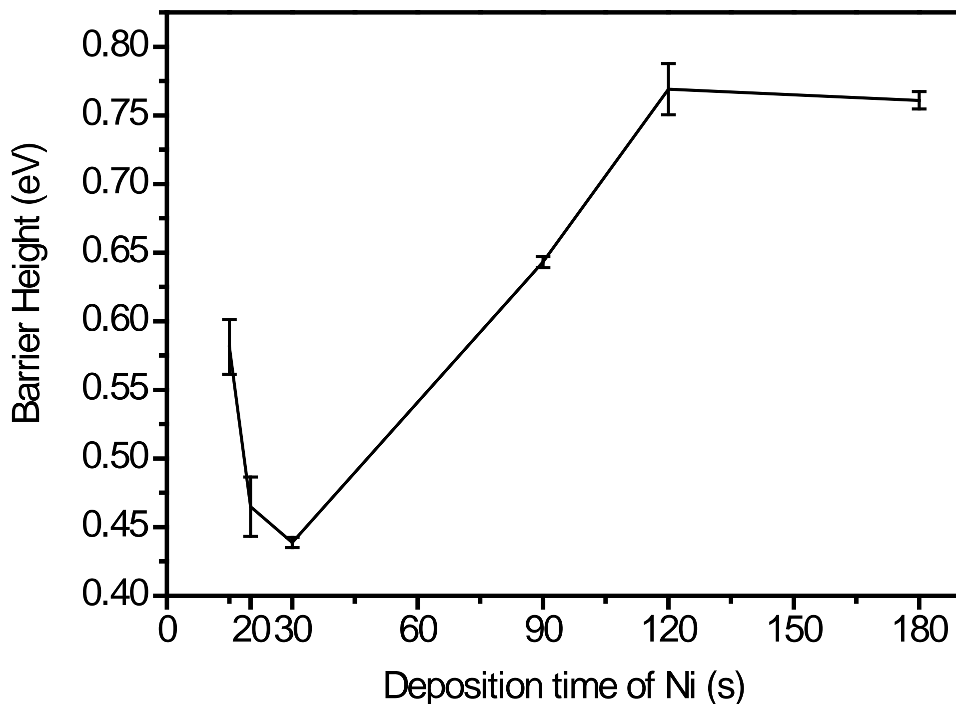

Figure 16 Graph depicting variation of ϕ_B against deposition time of Ni. ϕ_B is observed to reach a minimum of about 0.44eV at 30s of Ni deposition.

This suggests that a minimum of ϕ_B should be obtained for a deposition duration longer than 30s and shorter than 90s.

The trend corroborates that obtained from the ab-initio calculations presented in 6.4.1.2.1., with discussions on the trends done in 6.4.1.2.1 and 6.4.2.2. Furthermore, the values of ϕ_B obtained for longer deposition durations (120s and 180s) agree with similar results obtained by others. [15, 65]

6.4.3 Comparison of Empirical and Ab-initio Calculation Results

The trend for ϕ_B agrees well with results obtained from the ab-initio calculations, both of which indicating a higher ϕ_B at lower Ni coverage before decreasing to a minimum and then increasing with increasing Ni coverage, before stabilizing at the threshold for bulk Ni coverage.

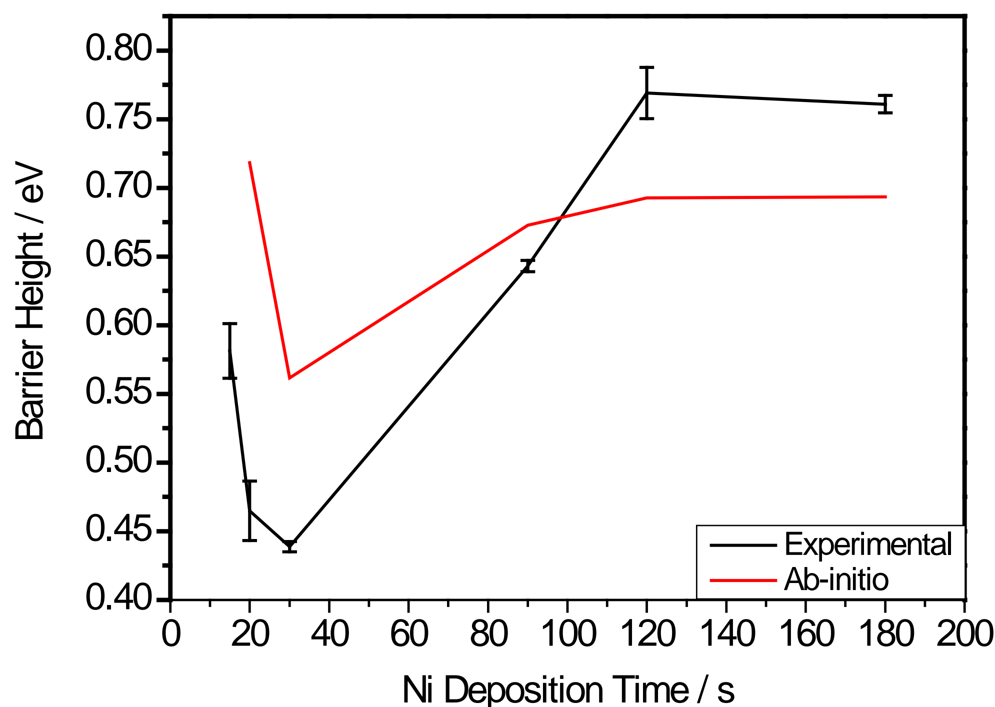

Figure 17 Estimating Ni deposition rate as 15s / ML, barrier height data from ab-initio calculations for 2MoS$_2$ series is matched with experimental results. The dampened fluctuation is expected due to the two extra layer of MoS$_2$ present [65], but in general, the trend proves our assumption in 6.4.1.2.1 correct.

It can be seen that the ab-initio data, which is obtained from the 2ML-MoS$_2$ series instead of the 1ML-MoS$_2$ series due to the latter's significant orbital hybridization that renders quantifying ϕ_B difficult, shows a dampened fluctuation as compared to the trend obtained from experimental data. This is expected due to the extra layer of MoS$_2$ present. [65]

By matching the two trends, we can also estimate the deposition rate of Ni to be about 15s / ML, which is as initially approximated in 6.4.2.1.

The use of ab-initio calculation, in addition to verifying our experimental results, has provided a theoretical explanation for the increase in barrier height with respect to increased nickel coverage. The minimum in barrier height is also observed in both ab-initio calculations as well as experimental results. Although more research is needed for a full explanation of the phenomenon, the extensive reconstruction and increased bonding between Ni and MoS_2 suggest interfacial interactions-induced events, such as fermi level pinning etc., are responsible it.

6.4.4 Results in Comparison with Those from Existing Research

The minimum empirically obtained barrier height of 0.45 eV is still inadequate, even when compared to the unsatisfactory 0.03eV barrier height of Sc-MoS_2 contact.

However, with the minimum barrier height about 50% that of bulk barrier height for the case of Ni-MoS_2, what this study demonstrates is that the barrier height of the metal contact can be effectively controlled by means of varying the coverage of the metal deposited. Assuming that other metal contact systems exhibit the same trend in barrier height – coverage variations as the Ni-MoS_2 system, the result is a significant one in terms of reducing barrier height for all metal contacts in general.

7 Conclusion

Monolayer MoS_2 has been successfully deposited using magnetron sputtering technique. The deposition conditions have been optimized to achieve the samples with good quality capable of producing significant photoluminescence. Effects of varying various deposition parameters are both theoretically analysed as well as experimentally

tested. Raman spectroscopy results confirm the capability of the magnetron sputtering technique in depositing monolayer scale films with good control. Photoluminescence reveals the presence of direct band gap monolayers whose Raman shift difference is larger than expected.

Empirical results corroborate Ab-initio simulation results for MoS_2-Ni contact systems and show that barrier height of the system varies with metal coverage. Strong interactions between Ni and MoS_2, leading to formation of NiS, are also observed.

8 Future Works

Various results observed require more in depth study that cannot be done here due to time limitations.

Firstly, Ab-initio results for 2ML-MoS_2-Ni systems showed a transition of the system from n-type to p-type and back to n-type with increasing nickel coverage. The emergence of a new valence band maximum for Ni coverage of around 2 and 3ML shows the possibility of modifying majority carrier type by varying metal coverage. However, the mechanism for this phenomenon needs to be studied before any useful application can be devised.

Secondly, monolayer Ni coverage is observed to lead to raised Schottky barrier height in both ab-initio simulations as well as experiments. The reason behind this sudden increase in barrier height is suspected to be the formation of NiS interface. However, as information of the electronic structure of NiS is scarce, more research into the band structure is needed to elucidate the real cause of the rise in barrier height for low Ni coverage.

Thirdly, it is observed that the minimum barrier height for the Ni-MoS_2 system is about 50% that of the bulk barrier height. However, whether this will hold for other metal-MoS_2 contacts is unknown. Similar studies using different metals is needed to verify that this encouraging result is valid for other systems as well.

Finally, due to the relocation of IMRE from NUS to OneNorth, device fabrication has not been successfully attempted. Measuring contact resistance, which is the most direct way of empirically finding the Schottky barrier height, has not been attempted. Due to the unavailability of the samples and equipment, coverage of the MoS_2 and the metal contact samples have not been verified using AFM or TEM. More confirmation is needed to verify the morphology, quality, and thickness of the deposited films.

9 References

1. Clark SJ, Segall MD, Pickard CJ, Hasnip PJ, Probert MJ, Refson K*, et al.* First principles methods using CASTEP. *Zeitschrift Fur Kristallographie* 2005, **220**(5-6)**:** 567-570.

2. Ding Y, Wang Y, Ni J, Shi L, Shi S, Tang W. First principles study of structural, vibrational and electronic properties of graphene-like MX2 (M=Mo, Nb, W, Ta; X=S, Se, Te) monolayers. *Physica B-Condensed Matter* 2011, **406**(11)**:** 2254-2260.

3. Eda G, Yamaguchi H, Voiry D, Fujita T, Chen M, Chhowalla M. Photoluminescence from Chemically Exfoliated MoS2. *Nano Letters* 2011, **11**(12)**:** 5111-5116.

4. Frey GL, Tenne R, Matthews MJ, Dresselhaus MS, Dresselhaus G. Optical properties of MS2 (M = Mo, W) inorganic fullerene-like and nanotube material optical absorption and resonance Raman measurements. *Journal of Materials Research* 1998, **13**(9)**:** 2412-2417.

5. Novoselov KS, Jiang D, Schedin F, Booth TJ, Khotkevich VV, Morozov SV*, et al.* Two-dimensional atomic crystals. *Proceedings of the National Academy of Sciences of the United States of America* 2005, **102**(30)**:** 10451-10453.

6. Lee C, Li Q, Kalb W, Liu X-Z, Berger H, Carpick RW*, et al.* Frictional Characteristics of Atomically Thin Sheets. *Science* 2010, **328**(5974)**:** 76-80.

7. Wang QH, Kalantar-Zadeh K, Kis A, Coleman JN, Strano MS. Electronics and optoelectronics of two-dimensional transition metal dichalcogenides. *Nature Nanotechnology* 2012, **7**(11)**:** 699-712.

8. Mak KF, Lee C, Hone J, Shan J, Heinz TF. Atomically Thin MoS2: A New Direct-Gap Semiconductor. *Physical Review Letters* 2010, **105**(13).

9. Hu KH, Hu XG, Sun XJ. Morphological effect of MoS2 nanoparticles on catalytic oxidation and vacuum lubrication. *Applied Surface Science* 2010, **256**(8)**:** 2517-2523.

10. Yin Z, Li H, Li H, Jiang L, Shi Y, Sun Y*, et al.* Single-Layer MoS2 Phototransistors. *Acs Nano* 2012, **6**(1)**:** 74-80.

11. Gourmelon E, Lignier O, Hadouda H, Couturier G, Bernède JC, Tedd J*, et al.* MS2 (M = W, Mo) photosensitive thin films for solar cells. *Solar Energy Materials and Solar Cells* 1997, **46**(2)**:** 115-121.

12. Ho WK, Yu JC, Lin J, Yu JG, Li PS. Preparation and photocatalytic behavior of MoS2 and WS2 nanocluster sensitized TiO2. *Langmuir* 2004, **20**(14)**:** 5865-5869.

13. Yoon Y, Ganapathi K, Salahuddin S. How Good Can Monolayer MoS2 Transistors Be? *Nano Letters* 2011, **11**(9)**:** 3768-3773.

14. Das S, Chen H-Y, Penumatcha AV, Appenzeller J. High Performance Multilayer MoS2 Transistors with Scandium Contacts. *Nano Letters* 2013, **13**(1)**:** 100-105.

15. Leong WS, Luo X, Li YD, Khoo KH, Quek SY, Thong JTL. Low Resistance Metal Contacts to MoS2 Devices with Nickel-Etched-Graphene Electrodes. *Acs Nano* 2015, **9**(1)**:** 869-877.

16. Vaziri S, Lupina G, Henkel C, Smith AD, Ostling M, Dabrowski J*, et al.* A Graphene-Based Hot Electron Transistor. *Nano Letters* 2013, **13**(4)**:** 1435-1439.

17. Lemme MC, Li L-J, Palacios T, Schwierz F. Two-dimensional materials for electronic applications. *Mrs Bulletin* 2014, **39**(8)**:** 711-718.

18. Lemme MC, Echtermeyer TJ, Baus M, Kurz H. A graphene field-effect device. *Ieee Electron Device Letters* 2007, **28**(4)**:** 282-284.

19. Kappera R, Voiry D, Yalcin SE, Branch B, Gupta G, Mohite AD*, et al.* Phase-engineered low-resistance contacts for ultrathin MoS2 transistors. *Nature Materials* 2014, **13**(12)**:** 1128-1134.

20. Voiry D, Yamaguchi H, Li JW, Silva R, Alves DCB, Fujita T*, et al.* Enhanced catalytic activity in strained chemically exfoliated WS2 nanosheets for hydrogen evolution. *Nature Materials* 2013, **12**(9)**:** 850-855.

21. Wypych F, Schollhorn R. 1T-MOS2, A NEW METALLIC MODIFICATION OF MOLYBDENUM-DISULFIDE. *Journal of the Chemical Society-Chemical Communications* 1992(19)**:** 1386-1388.

22. Tsai HL, Heising J, Schindler JL, Kannewurf CR, Kanatzidis MG. Exfoliated-restacked phase of WS2. *Chemistry of Materials* 1997, **9**(4)**:** 879-&.

23. Ambrosi A, Sofer Z, Pumera M. 2H [rightward arrow] 1T phase transition and hydrogen evolution activity of MoS2, MoSe2, WS2 and WSe2 strongly depends on the MX2 composition. *Chemical Communications* 2015, **51**(40)**:** 8450-8453.

24. Ma Y, Dai Y, Guo M, Niu C, Lu J, Huang B. Electronic and magnetic properties of perfect, vacancy-doped, and nonmetal adsorbed MoSe2, MoTe2 and WS2 monolayers. *Physical Chemistry Chemical Physics* 2011, **13**(34)**:** 15546-15553.

25. Kuc A, Zibouche N, Heine T. Influence of quantum confinement on the electronic structure of the transition metal sulfide. *Physical Review B* 2011, **83**(24)**:** 245213.

26. RadisavljevicB, RadenovicA, BrivioJ, GiacomettiV, KisA. Single-layer MoS2 transistors. *Nat Nano* 2011, **6**(3)**:** 147-150.

27. Castellanos-Gomez A, Barkelid M, Goossens AM, Calado VE, van der Zant HSJ, Steele GA. Laser-Thinning of MoS2: On Demand Generation of a Single-Layer Semiconductor. *Nano Letters* 2012, **12**(6)**:** 3187-3192.

28. Liu Y, Nan H, Wu X, Pan W, Wang W, Bai J*, et al.* Layer-by-layer thinning of MoS2 by plasma. *ACS Nano* 2013, **7**(5)**:** 4202-4209.

29. Utama MIB, Lu X, Zhan D, Ha ST, Yuan Y, Shen Z*, et al.* Etching-free patterning method for electrical characterization of atomically thin MoSe2 films grown by chemical vapor deposition. *Nanoscale* 2014, **6**(21)**:** 12376-12382.

30. Lu X, Utama MIB, Zhang J, Zhao Y, Xiong Q. Layer-by-layer thinning of MoS2 by thermal annealing. *Nanoscale* 2013, **5**(19)**:** 8904-8908.

31. Tao JG, Chai JW, Lu X, Wong LM, Wong TI, Pan JS*, et al.* Growth of wafer-scale MoS2 monolayer by magnetron sputtering. *Nanoscale* 2015, **7**(6)**:** 2497-2503.

32. Lin Y-C, Zhang W, Huang J-K, Liu K-K, Lee Y-H, Liang C-T*, et al.* Wafer-scale MoS2 thin layers prepared by MoO3 sulfurization. *Nanoscale* 2012, **4**(20)**:** 6637-6641.

33. Keune H, Lacom W, Rossi F, Stoffels E, Stoffels WW, Wahl G. Formation and deposition of MoS2-nanoparticles. *Journal De Physique Iv* 2000, **10**(P2)**:** 19-26.

34. Shi Y, Li H, Li L-J. Recent advances in controlled synthesis of two-dimensional transition metal dichalcogenides via vapour deposition techniques. *Chemical Society Reviews* 2015, **44**(9)**:** 2744-2756.

35. Najmaei S, Liu Z, Zhou W, Zou X, Shi G, Lei S*, et al.* Vapour phase growth and grain boundary structure of molybdenum disulphide atomic layers. *Nature Materials* 2013, **12**(8)**:** 754-759.

36. Ling X, Lee Y-H, Lin Y, Fang W, Yu L, Dresselhaus MS*, et al.* Role of the Seeding Promoter in MoS2 Growth by Chemical Vapor Deposition. *Nano Letters* 2014, **14**(2)**:** 464-472.

37. Gronborg SS, Ulstrup S, Bianchi M, Dendzik M, Sanders CE, Lauritsen JV*, et al.* Synthesis of Epitaxial Single-Layer MoS2 on Au(111). *Langmuir* 2015, **31**(35)**:** 9700-9706.

38. Liu K-K, Zhang W, Lee Y-H, Lin Y-C, Chang M-T, Su C*, et al.* Growth of Large-Area and Highly Crystalline MoS2 Thin Layers on Insulating Substrates. *Nano Letters* 2012, **12**(3)**:** 1538-1544.

39. Tao J, Chai J, Lu X, Wong LM, Wong TI, Pan J*, et al.* Growth of wafer-scale MoS2 monolayer by magnetron sputtering. *Nanoscale* 2015, **7**(6)**:** 2497-2503.

40. Kang K, Xie S, Huang L, Han Y, Huang PY, Mak KF*, et al.* High-mobility three-atom-thick semiconducting films with wafer-scale homogeneity. *Nature* 2015, **520**(7549)**:** 656-660.

41. Lee Y-H, Zhang X-Q, Zhang W, Chang M-T, Lin C-T, Chang K-D*, et al.* Synthesis of Large-Area MoS2 Atomic Layers with Chemical Vapor Deposition. *Advanced Materials* 2012, **24**(17)**:** 2320-2325.

42. Song J-G, Park J, Lee W, Choi T, Jung H, Lee CW*, et al.* Layer-Controlled, Wafer-Scale, and Conformal Synthesis of Tungsten Disulfide Nanosheets Using Atomic Layer Deposition. *Acs Nano* 2013, **7**(12)**:** 11333-11340.

43. Jeon J, Jang SK, Jeon SM, Yoo G, Jang YH, Park J-H*, et al.* Layer-controlled CVD growth of large-area two-dimensional MoS2 films. *Nanoscale* 2015, **7**(5)**:** 1688-1695.

44. Bilgin I, Liu F, Vargas A, Winchester A, Man MKL, Upmanyu M*, et al.* Chemical Vapor Deposition Synthesized Atomically Thin Molybdenum Disulfide with Optoelectronic-Grade Crystalline Quality. *Acs Nano* 2015, **9**(9)**:** 8822-8832.

45. Kasap S. *Principles of Electronic Materials and Devices*, 3 edn. McGraw-Hill Education, 2005.

46. Gong C, Colombo L, Wallace RM, Cho K. The Unusual Mechanism of Partial Fermi Level Pinning at Metal-MoS2 Interfaces. *Nano Letters* 2014, **14**(4)**:** 1714-1720.

47. Kaushik N, Nipane A, Basheer F, Dubey S, Grover S, Deshmukh MM*, et al.* Schottky barrier heights for Au and Pd contacts to MoS2. *Applied Physics Letters* 2014, **105**(11).

48. Fang H, Tosun M, Seol G, Chang TC, Takei K, Guo J*, et al.* Degenerate n-Doping of Few-Layer Transition Metal Dichalcogenides by Potassium. *Nano Letters* 2013, **13**(5)**:** 1991-1995.

49. Du Y, Liu H, Neal AT, Si M, Ye PD. Molecular Doping of Multilayer MoS2 Field-Effect Transistors: Reduction in Sheet and Contact Resistances. *Ieee Electron Device Letters* 2013, **34**(10)**:** 1328-1330.

50. Chen J-R, Odenthal PM, Swartz AG, Floyd GC, Wen H, Luo KY*, et al.* Control of Schottky Barriers in Single Layer MoS2 Transistors with Ferromagnetic Contacts. *Nano Letters* 2013, **13**(7)**:** 3106-3110.

51. Liu Y, Wu H, Cheng H-C, Yang S, Zhu E, He Q*, et al.* Toward Barrier Free Contact to Molybdenum Disulfide Using Graphene Electrodes. *Nano Letters* 2015, **15**(5)**:** 3030-3034.

52. Suh J, Park T-E, Lin D-Y, Fu D, Park J, Jung HJ*, et al.* Doping against the Native Propensity of MoS2: Degenerate Hole Doping by Cation Substitution. *Nano Letters* 2014, **14**(12)**:** 6976-6982.

53. Li H, Zhang Q, Yap CCR, Tay BK, Edwin THT, Olivier A*, et al.* From Bulk to Monolayer MoS2: Evolution of Raman Scattering. *Advanced Functional Materials* 2012, **22**(7)**:** 1385-1390.

54. Lee C, Yan H, Brus LE, Heinz TF, Hone J, Ryu S. Anomalous Lattice Vibrations of Single- and Few-Layer MoS2. *Acs Nano* 2010, **4**(5)**:** 2695-2700.

55. Splendiani A, Sun L, Zhang YB, Li TS, Kim J, Chim CY*, et al.* Emerging Photoluminescence in Monolayer MoS2. *Nano Letters* 2010, **10**(4)**:** 1271-1275.

56. Hohenberg P, Kohn W. Inhomogeneous Electron Gas. *Physical Review* 1964, **136**(3B)**:** B864-B871.

57. Kohn W, Sham LJ. Self-Consistent Equations Including Exchange and Correlation Effects. *Physical Review* 1965, **140**(4A)**:** A1133-A1138.

58. Lee JG. *Computational Materials Science: An Introduction*, 1 edn. CRC Press, 2011.

59. Baker BG, Johnson BB, Maire GLC. Photoelectric work function measurements on nickel crystals and films. *Surface Science* 1971, **24**(2)**:** 572-586.

60. Wendt AE, Lieberman MA. Spatial structure of a planar magnetron discharge. *Journal of Vacuum Science & Technology A* 1990, **8**(2)**:** 902-907.

61. Depla D, Mahieu S. *Reactive Sputter Deposition*. Springer-Verlag Berlin Heidelberg, 2008.

62. Mignuzzi S, Pollard AJ, Bonini N, Brennan B, Gilmore IS, Pimenta MA*, et al.* Effect of disorder on Raman scattering of single-layer. *Physical Review B* 2015, **91**(19)**:** 195411.

63. Zhan YJ, Liu Z, Najmaei S, Ajayan PM, Lou J. Large-Area Vapor-Phase Growth and Characterization of MoS2 Atomic Layers on a SiO2 Substrate. *Small* 2012, **8**(7)**:** 966-971.

64. Lin MW, Liu LZ, Lan Q, Tan XB, Dhindsa KS, Zeng P*, et al.* Mobility enhancement and highly efficient gating of monolayer MoS2 transistors with polymer electrolyte. *Journal of Physics D-Applied Physics* 2012, **45**(34).

65. Zhong H, Quhe R, Wang Y, Ni Z, Ye M, Song Z*, et al.* Interfacial Properties of Monolayer and Bilayer MoS2 Contacts with Metals: Beyond the Energy Band Calculations. *Scientific Reports* 2016, **6:** 21786.

66. Liang KS, Hughes GJ, Chianelli RR. UPS investigation of poorly crystallized MoS2. *Journal of Vacuum Science & Technology A* 1984, **2**(2)**:** 991-994.

67. Kraut EA, Grant RW, Waldrop JR, Kowalczyk SP. PRECISE DETERMINATION OF THE VALENCE-BAND EDGE IN X-RAY PHOTOEMISSION SPECTRA - APPLICATION TO MEASUREMENT OF SEMICONDUCTOR INTERFACE POTENTIALS. *Physical Review Letters* 1980, **44**(24)**:** 1620-1623.